Crystal Plasticity Modeling of Deformation and Creep in Polycrystalline Ti-6242

DHYANJYOTI DEKA, DEEPU S. JOSEPH, SOMNATH GHOSH, and MICHAEL J. MILLS

This paper develops an experimentally validated computational model based on crystal plasticity for the analysis of two-phase α/β Ti-6242 polycrystalline alloys. A rate-dependent elastic-crystal plasticity model is incorporated in this model to accommodate anisotropy in material behavior and tension-compression asymmetry inherent to this alloy. A combination of microtesting, orientation imaging microscopy, computational simulations, and minimization process, involving genetic algorithms, is implemented in this study for careful characterization and calibration of the material parameters. Size effects are considered in this analysis through a simple scaling process. A homogenized equivalent model of the primary α with transformed β colonies is developed for incorporation in the Ti-6242 FE model. The polycrystalline Ti-6242 computational model incorporates accurate phase volume fractions, as well as statistically equivalent orientation distributions to those observed in the orientation imaging microscopy scans. The effects of orientation, misorientations, and microtexture distributions are investigated through simulations by this computational model. The model is used to simulate constant strain rate and creep tests in compression and tension, and the results are compared with experiments. The effects of microstructure and creep-induced load-shedding on the localization of microstructural stresses and strains are studied for potential crack initiation criteria.

I. INTRODUCTION

TWO-PHASE α/β titanium alloys are widely used in a number of high-performance aerospace, orthopaedic, dental, and sporting goods applications[1] on account of their desirable properties, such as high specific strength, elastic modulus, and fracture toughness. These alloys are created from allotropic transformation of pure titanium from hcp to bcc structures at around the phase transition temperature ($\sim$882 °C). Despite the desirable properties, the performance of Ti alloys is sometimes hindered due to creep at low temperatures ($T/T_m < 0.2$) and at a fraction of the yield strength.[2–5] Significant creep strains have been experimentally reported to accumulate at applied stresses as low as 60 pct of the yield strength.[4] Consequently, sufficient caution must be exercised in the application of these alloys where dimensional tolerance is a critical factor.

The low-temperature strain rate sensitivity and creep behavior of Ti alloys are very different from most other metallic alloys.[6] Transmission electron microscopy (TEM) study has shown that deformation actually proceeds via dislocation glide, where the dislocations are inhomogeneously distributed into planar arrays. Planarity of slip has been attributed to the effect of short range order (SRO) of Ti and Al atoms on the hcp lattice.[7] The creep process is of a transient kind or "exhaustion" type where the creep rate continually decreases with time.[2–5] This "cold" creep characteristic has previously been attributed to rate sensitivity effects.[8] The creep in two-phase α/β Ti alloys has also been observed to be strongly dependent on the microstructure,

with creep resistance decreasing as the colony size increases.[5]

Plastic deformation in Ti alloys has considerable dependence on the grain orientation due to the low symmetry of the predominant hcp α phase. Differences in slip system deformation resistance of the individual slip systems result in a highly anisotropic behavior.[9] Grains with their [0001] crystal orientation close to the deformation axis ($<\mathbf{c} + \mathbf{a}>$ oriented) are significantly stronger than other grains. This is because in the [0001] orientation, $<\mathbf{c} + \mathbf{a}>$ dislocation slip on pyramidal slip systems are activated that have a much higher critical resolved shear strength (CRSS) than the $<\mathbf{a}>$ type slip on basal or prismatic planes. Large local stress concentrations arise in these $<\mathbf{c} + \mathbf{a}>$ oriented grains due to local load shedding from neighboring softer grains, and hence the local grain morphology is of considerable importance in crack initiation in Ti alloys. Recently, it has been revealed that crack initiation in Ti alloys is associated with grains that have their [0001] crystal orientations close to the deformation axis.[10,11,12]

This paper invokes a combination of experiments and finite element-based simulations to develop a physically based rate-dependent crystal-plasticity model for predicting deformation and creep behavior of two phase Ti-6Al-2Sn-4Zr-2Mo or Ti-6242 alloy (Table I lists composition). A special focus is on understanding the effect of microstructural orientation distribution on this behavior. Crystal-plasticity models have been developed by a number of researchers for modeling anisotropic material behavior.[13–16] Anand *et al.* have developed crystal-plasticity computational models from experimental data for fcc, bcc, and hcp metals.[9,17,18] Grujicic *et al.*[19] have modeled room-temperature behavior of twinned γ-TiAl + α_2-Ti$_3$Al single crystals using a rate-dependent crystal-plasticity model, while 2D models of this material have been developed by Kad *et al.*[20] A number of very interesting recent papers have also emerged on the subject.[21–25] The modeling of twinning behavior in hcp crystals using a rate-independent model is discussed in

DHYANJYOTI DEKA and DEEPU S. JOSEPH, Graduate Students, and SOMNATH GHOSH, Professor, are with the Department of Mechanical Engineering, The Ohio State University, Columbus, OH. Contact e-mail: ghosh.5@osu.edu MICHAEL J. MILLS, Professor, is with the Department of Materials Science and Engineering, The Ohio State University, Columbus, OH.
Manuscript submitted September 7, 2005.

Table I. Chemical Composition of Ti-6242

Alloy	Al (Wt Pct)	Mo (Wt Pct)	Sn (Wt Pct)	Zr (Wt Pct)	Si (Wt Pct)	O (Wt Pct)	N (Wt Pct)	Ti (Wt Pct)
Ti -6242	6.01	1.96	1.96	4.01	0.10	0.131	0.012	85.82

Staroselsky and Anand.[21] Diard *et al.*[22] have developed a 3D model of polycrystalline materials from Voronoi tessellation and used a rate-dependent crystal-plasticity model to simulate the behavior of a zirconium alloy in both constant strain rate and creep tests. A 3D fcc polycrystalline microstructure was created using the Potts model by Buchheit *et al.*,[23] which is used for texture evolution. The distribution of elastic strains following plastic deformation of an aluminum alloy was evaluated by FEM simulations in the orientation space by Loge *et al.*[24] and compared with results from neutron diffraction experiments. Li *et al.*[25] have used crystal-plasticity modeling to study the evolution of crystallographic textures during cold rolling of hot-rolled aluminum plates in comparison with fully constrained Taylor model. Recently, Salem *et al.*[26] have developed relations for the evolution of slip and twin resistance based on experiments. In a preceding paper by the authors of this paper, Hasija *et al.*[27] have developed an experimentally validated crystal-plasticity model of Ti-6Al with a focus on load shedding at the interfaces between hard and soft grains.

As a sequel to the earlier work on crystal-plasticity modeling for pure Ti-6Al alloys by the authors,[27] the present paper presents a systematic approach to develop an experimentally calibrated and validated computational model for α/β Ti-6242 alloys. The computational model takes into account the individual primary α and transformed β phases in the alloy and incorporates experimentally observed phenomena of material anisotropy, large strains, time-dependent plasticity, and tension-compression asymmetry. A homogenized transformed β model incorporating the individual volume fractions of the α/β lath structure in the colonies is developed following the rule of mixtures. The equivalent model takes into account the deformation produced by multiple slip systems in the α and β phases. A systematic approach is followed for calibrating the crystal-plasticity parameters of each of the constituent phases in Ti-6242 microstructure, using a genetic algorithm (GA)-based optimization scheme.[16] This scheme minimizes the difference in specific properties obtained by experiments and simulation. Tests with single crystals of α-Ti-6Al and single colonies of α/β transformed β are conducted to provide the necessary experimental data. Initial guesses for the material parameters are taken from previous results.[27] Upon adequate material characterization of individual phases, models of polycrystalline-polyphase Ti-6242 are constructed and simulated for validation. These computational models incorporate effective volume fractions of individual phases, as well as crystallographic orientation distributions, based on microstructural data obtained by orientation imaging microscopy (OIM). Specifically, three variants of statistically equivalent orientation distributions are considered in the computational model of the polycrystalline-polyphase aggregate: (1) equivalent orientation distribution (OD) based on population fraction of orientations, (2) equivalent orientation and misorientation distribution (MOD) based on population fraction of misorientations, and (3) equivalent
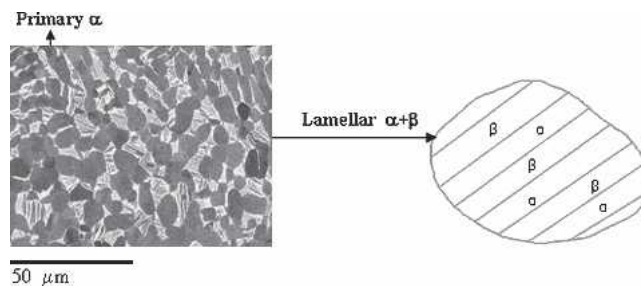

Fig. 1—(*a*) Microstructure of a forged $\alpha + \beta$ Ti-6242 alloy consisting of transformed β (dark phase) colonies in a matrix of equiaxed primary α grains (light phase). (*b*) Schematic of a constituent transformed β colony.

microtexture distribution based on local volume fraction of orientations. Results of the polycrystalline model simulations for constant strain rate and creep tests are compared with experiments for validation of the overall model.

The final task in this paper is to understand the effect of the local microstructure and loading on the evolution of local stresses and strains in creep. This is the first step toward identifying a crack nucleation criterion for the material.

II. MATERIALS

An optical micrograph of a forged Ti-6242 material is shown in Figure 1. The microstructure consists of regions of transformed β colonies in a matrix of equiaxed primary α-Ti-6Al grains. The primary α grains have an hcp structure, whereas the transformed β colonies consist of alternating α (hcp) and β (bcc) laths (Figure 2). For hcp lattice structure, the material basis vectors are denoted by a set of nonorthogonal base vectors $\{a_1, a_2, a_3, c\}$ with the constraint $a_1 + a_2 + a_3 = 0$.[9] As shown in Figure 2(a), the hcp crystals consist of five different families of slip systems —the basal $<a>$, prismatic $<a>$, pyramidal $<a>$, first-order pyramidal $<c + a>$, and second-order pyramidal $<c + a>$—with a total of 30 possible slip systems. A transversely isotropic elastic response is assumed for these crystals with five independent constants. The bcc crystal systems in Figure 2(b) consist of three different slip families —$<111>\{110\}$, $<111>\{112\}$, and $<111>\{123\}$—with the unit cell defined by three lattice vectors in a cartesian coordinate system $\{e_1^c, e_2^c, e_3^c\}$. A cubic symmetric elastic matrix is assumed for the bcc material with three independent constants.

The volume fraction of the transformed β phase in the overall Ti-6242 microstructure that is analyzed is about 30 pct, whereas that for the primary α phase is approximately 70 pct. The volume fractions depend on the temperature at which the hot working takes place. Within the transformed β colonies themselves, α and β lamellae were experimentally observed to have volume fractions of approximately 88 pct and 12 pct, respectively.[28] The orientations of the α and β lamellae follow a specific relation given by
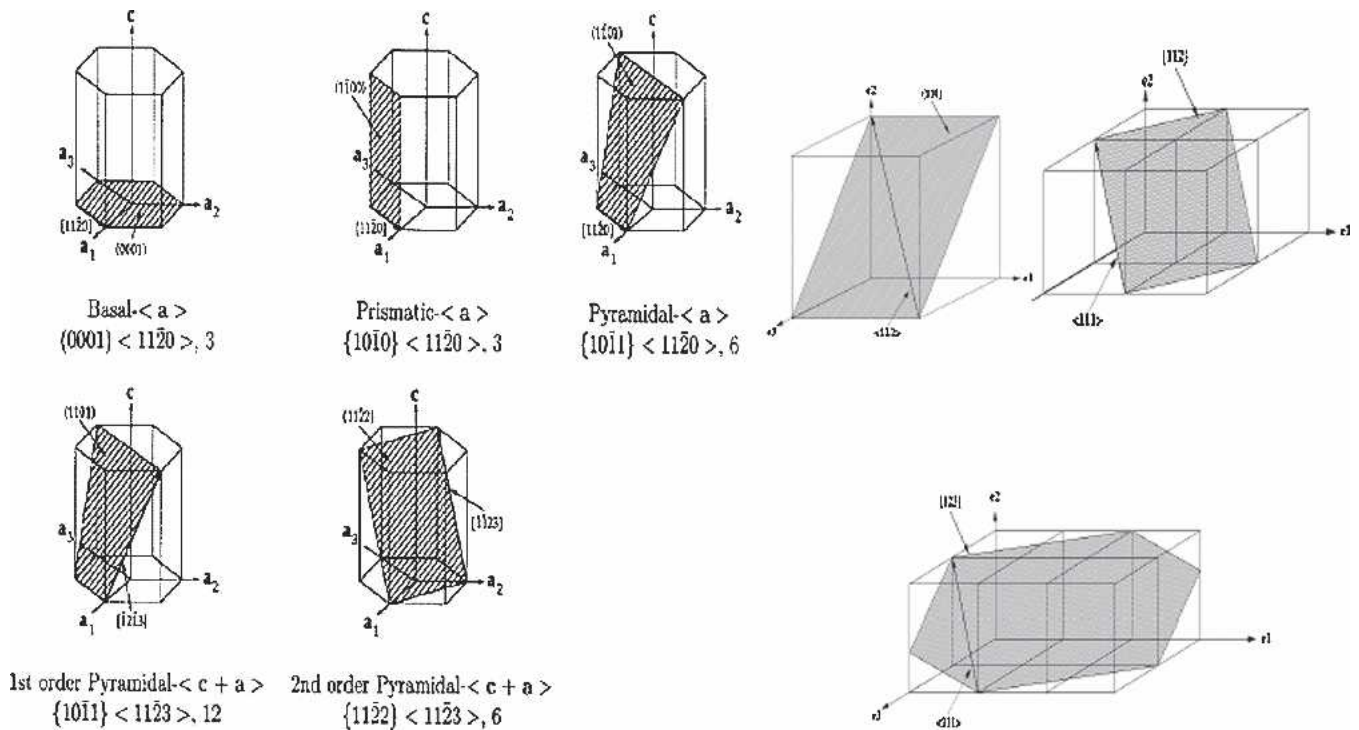
Fig. 2—Schematic diagrams showing (*a*) the nonorthogonal basis and slip systems in an hcp crystal and (*b*) the orthogonal basis and slip systems in bcc crystals.

the Burger's orientation relationship,[29] expressed as $(101)_\beta \| (0001)_\alpha$, $[1\bar{1}\bar{1}]_\beta \| [2\bar{1}\bar{1}0]_\alpha$. This relation brings the *hcp* a_1 ($[2\bar{1}\bar{1}0]$) slip direction into coincidence with the *bcc* b_1 slip direction. OIM images show that there is a very small misalignment of ~0.56 deg between the a_1 and b_1 slip directions for this alloy. However, there is a significant misalignment between the α phase a_2 ($[\bar{1}2\bar{1}0]$) and β phase b_2 slip directions. Also, the a_3 ($[\bar{1}\bar{1}20]$) direction is not closely aligned with any $<111>_\beta$ direction in the β phase at all. Consequently, the ease of α/β slip transmission for a_1, a_2, and a_3 basal and prismatic slips varies significantly. Significant tension-compression asymmetry is also observed in the single colonies of α/β Ti 6242. Experimental studies[28] have attributed this behavior to one or a combination of (1) residual stresses in single colony due to growth process, (2) generation of elastic stress fields at the α/β interface aiding or impairing slip transmission, (3) effects on the mobility of $<a>$ type dislocations in the α phase, and (4) effects on the mobility of dislocations in the β phase and differing slip transmission mechanisms based on the direction of loading.

III. CONSTITUTIVE MODEL

The deformation behavior of individual phases of the Ti-6242 microstructure is modeled using a rate-dependent, isothermal, elastic-plastic, finite strain, crystal-plasticity formulation, following the model previously proposed.[9,17,30] The model does not account for microtwinning because this mechanism has not been observed in associated experiments.[28,29] The general framework for the crystal-plasticity formulation is taken to be the same for both the hcp and bcc phases, with the only difference introduced in the hardening laws.

In this model, crystal deformation results from a combination of the elastic stretching and rotation of the crystal lattice and plastic slip on the different slip systems. The stress-strain relation in this model is written in terms of the second Piola-Kirchoff stress ($\mathbf{S} = \det\mathbf{F}^e \ \mathbf{F}^{e-1} \ \boldsymbol{\sigma} \ \mathbf{F}^{e-T}$) and the work conjugate Lagrange Green strain tensor ($\mathbf{E}^e \equiv (1/2)$ $\{\mathbf{F}^{eT}\mathbf{F}^e - \mathbf{I}\}$) as

$$\mathbf{S} = C{:}\mathbf{E}^e \qquad [1]$$

where C = the fourth-order anisotropic elasticity tensor, $\boldsymbol{\sigma}$ = the Cauchy stress tensor, and $\mathbf{F}^e$ = the elastic deformation gradient defined by the relation

$$\mathbf{F}^e \equiv \mathbf{F} \ \mathbf{F}^{p-1}, \ \det\mathbf{F}^e > 0 \qquad [2]$$

$\mathbf{F}$ and $\mathbf{F}^p$ represent the deformation gradient and its plastic component, respectively, with the incompressibility constraint $\det\mathbf{F}^p = 1$. The flow rule governing evolution of plastic deformation is expressed in terms of the plastic velocity gradient as:

$$\mathbf{L}^p = \dot{\mathbf{F}}^p \mathbf{F}^{p-1} = \sum_\alpha \dot{\gamma}^\alpha \mathbf{s}_0^\alpha \qquad [3]$$

where the Schmid tensor is expressed as $\mathbf{s}_0^\alpha \equiv \mathbf{m}_0^\alpha \otimes \mathbf{n}_0^\alpha$ in terms of the slip direction ($\mathbf{m}_0^\alpha$) and slip plane normal ($\mathbf{n}_0^\alpha$) in the reference configuration, associated with α^{th} slip system. The plastic shearing rate $\dot{\gamma}^\alpha$ on the αth slip system is given by the power law relation,[17,20] given as

$$\dot{\gamma}^\alpha = \dot{\tilde{\gamma}} \left| \frac{\tau^\alpha}{g^\alpha} \right|^{1/m} \mathrm{sign}(\tau^\alpha), \ \tau^\alpha \equiv (\boldsymbol{C}^e : \mathbf{S}) \cdot \mathbf{s}_0^\alpha \qquad [4]$$

Here $\dot{\tilde{\gamma}}$ is the reference plastic shearing rate, τ^α and g^α = the αth slip system resolved shear stress and the slip system deformation resistance, respectively, m = the material rate sensitivity parameter, and $\boldsymbol{C}^e$ = the elastic stretch. The slip system resistance is taken to evolve as:

$$\dot{g}^\alpha = \sum_{\beta=1}^{\mathrm{nslip}} h^{\alpha\beta} |\dot{\gamma}^\beta| = \sum_\beta q^{\alpha\beta} h^\beta |\dot{\gamma}^\beta| \qquad [5]$$

where $h^{\alpha\beta}$ = the strain hardening rate due to self and latent hardening, h^β = the self-hardening rate, and $q^{\alpha\beta}$ = a matrix describing the latent hardening. For the hcp phase, the evolution of the self-hardening rate is assumed to be governed by the relation:[18,27]

$$h^\beta = h_0^\beta \left| 1 - \frac{g^\beta}{g_s^\beta} \right|^r \mathrm{sign}\left(1 - \frac{g^\beta}{g_s^\beta} \right), \ g_s^\beta = \tilde{g}\left(\frac{\dot{\gamma}^\beta}{\dot{\tilde{\gamma}}} \right)^n \qquad [6]$$

where h_0^β is the initial hardening rate, g_s^β is the saturation slip deformation resistance, and r, $\tilde{g}$, and n = the slip system hardening parameters. A different relation has been proposed for the evolution of the self-hardening rate for bcc materials,[31] as

$$h^\beta = h_s^\beta + \mathrm{sech}^2 \left[\left(\frac{h_0^\beta - h_s^\beta}{\tau_s^\beta - \tau_0^\beta} \right) \gamma_\alpha \right] (h_0^\beta - h_s^\beta),$$

$$\gamma_\alpha = \int_0^t \sum_{\beta=1}^{\mathrm{nslip}} |\dot{\gamma}^\beta| \, dt \qquad [7]$$

where h_0^β and h_s^β are the initial and asymptotic hardening rates, τ_s^β represent the saturation value of the shear stress when $h_s^\beta = 0$, and γ_a = a measure of total plastic shear. This relation is assumed to govern the hardening evolution in the bcc phase of the transformed β colonies. Since cyclic deformation is not modeled in this paper, the explicit incorporation of kinematic hardening is not discussed. The crystal-plasticity model is incorporated in the commercial finite element code ABAQUS[32] using the user-defined material routine UMAT. An implicit time integration scheme[17,18] was used to integrate the crystal plasticity Eqs. [1] through [7]. Known deformation variables like the deformation gradient $\mathbf{F}(t)$, the plastic deformation gradient $\mathbf{F}^p(t)$, the slip system deformation resistance $s^\alpha(t)$ at time t, and the deformation gradient $\mathbf{F}(t + \Delta t)$ at $t + \Delta t$ are passed to the material update routine in UMAT. The integration algorithm in the UMAT subroutine updates stresses, plastic strains, and all slip system internal variables to the end of the time step at $t + \Delta t$. Explicit discussion of this implementation has been presented.[16,27]

IV. EXPERIMENTS ON SINGLE COLONIES AND POLYCRYSTALLINE TI-6242

Mechanical tests on α-phase single crystals and single $\alpha - \beta$ colony crystals provide data for calibration of

material parameters and validation of the computational model. Previously,[27] the authors have described detailed mechanical testing of single-crystal and polycrystalline Ti-6Al alloys. Tests of Ti-6242 single colonies in compression[33] and in tension[34,35] have also been conducted. The salient details of these experiments and the resulting flow curves are described below. In addition, tests on polycrystalline Ti-6242 consisting of primary α and transformed β phases[36] are used to validate the model being developed. These individual experiments are briefly summarized below.

A. Microscopy and Mechanical Testing of Single α/β Colonies in Ti-6242 Microstructure

Single α/β colonies of Ti-6242 are grown using a vertical float zone technique in a Crystalox furnace at the Air Force Research Labs in Wright-Patterson Air Force Base. All samples for mechanical testing are extracted from successfully grown colonies ranging in size from 5 to 25 mm. Laue back-reflection X-ray techniques are used to identify the crystallographic orientation of the α phase. Scanning electron microscopy (SEM) observations are used to determine the relative alignment of the broad face of the α/β interface, allowing for the unambiguous identification of the three $\boldsymbol{a}$-type $\{11\bar{2}0\}$ slip directions. Thin sections are cut from the single colony rod using a slow-speed diamond saw. A plunge electrical discharge machining (EDM) process is used to extract dogbone-shaped microtensile samples from the thin oriented single-crystal sections. To activate a specific slip system and allow for direct observation of β lath shearing on the sample surface, the thin sections are extracted such that the desired Burger's vector is contained in the section and oriented 45 deg from the tensile axis. Microtensile testing of these samples is performed in a piezo-driven microsample testing machine. Six tests are conducted at a constant strain rate of 1.0×10^{-4} s^{-1} with maximum slip activity on the $\boldsymbol{a_1}$, $\boldsymbol{a_2}$, and $\boldsymbol{a_3}$ basal and prismatic slip systems. Similarly, compression test samples in the form of $3 \times 3 \times 8$-mm rectangular bars are sectioned from the single colony rod, and imaging is carried out. The compression samples are each oriented to maximize the resolved shear stress on one of the three $\boldsymbol{a}$-type slip directions on the basal plane ($\boldsymbol{a_1}$, $\boldsymbol{a_2}$, $\boldsymbol{a_3}$). Table II lists the Schmid factor for each orientation for the three $\boldsymbol{a}$-type slip directions on basal, prismatic, or first-order pyramidal planes. Compression testing at a constant strain rate of 1×10^{-4} s^{-1} is performed at room temperature using an INSTRON* 1362 mechanical test frame equipped with

---

---

a compression cage.

B. Mechanical Testing of Ti-6242 Polycrystals

Compression tests on polycrystalline Ti-6242 are performed on rectangular samples of nominal dimension $4 \times 4 \times 12$ mm. These samples are attached to strain gages of strain resolution of 10^{-6}. Constant strain rate samples were tested at room temperature at 1×10^{-4} s^{-1} using an Instron 1362 mechanical test frame equipped with a compression cage. Creep samples are tested using an ATS 20 kips dead load creep frame at a stress that is 95.5 pct of the engineering

Table II. Schmid Factor on Different Slip Planes for Six Different Orientations

Slip System	a_1 Basal ($2\bar{1}\bar{1}3$)	a_2 Basal ($\bar{1}2\bar{1}3$)	a_3 Basal ($\bar{1}\bar{1}23$)	a_1 Prismatic ($3\bar{4}10$)	a_2 Prismatic ($\bar{3}410$)	a_3 Prismatic ($1\bar{4}30$)
Basal						
a/3[$\bar{2}110$](0001)	0.50	0.25	0.25	0.00	0.00	0.00
a/3[$\bar{1}2\bar{1}0$](0001)	0.25	0.50	0.25	0.00	0.00	0.00
a/3[$\bar{1}\bar{1}20$](0001)	0.25	0.25	0.50	0.00	0.00	0.00
Prismatic						
a/3[$\bar{2}110$]($01\bar{1}0$)	0.00	0.23	0.23	0.50	0.26	0.26
a/3[$\bar{1}2\bar{1}0$]($10\bar{1}0$)	0.23	0.00	0.23	0.26	0.50	0.23
a/3[$\bar{1}\bar{1}20$]($\bar{1}100$)	0.23	0.23	0.00	0.23	0.23	0.50
Pyramidal						
a/3[$\bar{2}110$]($0\bar{1}11$)	0.24	0.32	0.32	0.44	0.23	0.21
a/3[$\bar{2}110$]($0\bar{1}1\bar{1}$)	0.24	0.08	0.08	0.44	0.23	0.21
a/3[$\bar{1}2\bar{1}0$]($10\bar{1}1$)	0.32	0.24	0.32	0.23	0.44	0.20
a/3[$\bar{1}2\bar{1}0$]($\bar{1}011$)	0.08	0.24	0.08	0.25	0.44	0.24
a/3[$\bar{1}2\bar{1}0$]($1\bar{1}01$)	0.32	0.32	0.24	0.20	0.20	0.44
a/3[$\bar{1}\bar{1}20$]($1\bar{1}0\bar{1}$)	0.08	0.08	0.24	0.17	0.20	0.44

Table III. Components of Elasticity Matrix in the Material Coordiantes for hcp and bcc Phases in the Ti-6242 Microstructure

Phase	$C_1 = C_{22}$ (GPa)	C_{33} (GPa)	C_{12} (GPa)	$C_{13} = C_{23}$ (GPa)	C_{44} (GPa)	$C_{55} = C_{66}$ (GPa)	Other C_{ab} (GPa)
hcp (transversely isotropic)	170.0	204.0	98.0	86.0	36.0	51.0	0.0
bcc (cubic symmetry)	250.2	250.2	19.0	19.0	115.3	115.3	0.0

yield stress of 907 MPa. The tensile constant strain rate experiments are done at 1.114×10^{-4} s^{-1} in a closed-loop servohydraulic test frame. The specimens are of uniform circular cross-section with a gage section diameter of 6.35 mm, reduced section length of 31.75 mm, and threaded grip section diameter of 9.52 mm. The tensile dead load creep test is performed at an engineering stress of 897 MPa. Specimens are of uniform circular cross-section with a gage section diameter of 5.08 mm, reduced section length of 19.05 mm, and threaded grip section of diameter of 15.88 mm. More details of these tests have been previously provided.[36]

V. DETERMINATION OF MATERIAL PARAMETERS FROM EXPERIMENTAL DATA

Systematic calibration of material parameters from experimental results is a nontrivial effort owing to the heterogeneity in the microstructure and the number of parameters involved. Together with the description of slip system orientations and geometry and loading conditions, these parameters define inputs to the computational model for the deformation analysis, consistent with experiments. The material parameters to be calibrated include (1) the set $C_{\alpha\beta}$ ($\alpha = 1...6$, $\beta = 1...6$) of anisotropic elastic stiffness components, (2) the set of flow-related parameters, $\tilde{\gamma}$, g^α, m, and (3) the set of hardening evolution-related parameters h_0, h_s, τ_0, τ_s, r, n, $\tilde{g}$ in the hcp and bcc phases as discussed in Eqs. [1] through [7]. A genetic algorithm (GA)-based technique[16,37] is used in the calibration process to perform a least square minimization of the difference between the experimental and simulation material properties. Genetic algorithms are discrete function minimization techniques based on the mechanism of natural selection and natural

genetics.[37,38] GA starts with a set of random solutions and the discrete design parameters evolve through the generations to an optimized set using three genetic operators: reproduction, crossover, and mutation. In this problem, the minimization of the fitness or objective function for GA is stated as

$$\underset{\text{design material parameters } \nu}{\text{Minimize}} : f = \sum_{i=1}^{nd} \left\| \sigma_i^{\text{experimental}} - \sigma_i^{\text{simulated}}(\varepsilon_i^{\text{experimental}}, \nu) \right\|^2 \quad [8]$$

where nd = the number of data points at which the variables are calculated and ν = the set of material parameters to be calibrated. It should be noted that the parameters evaluated by this method are nonunique due to the highly nonlinear crystal-plasticity equations. This is a limitation of this calibration process, and the effectiveness of parameters can be established only through tests at multiple scales. While this paper considers only macroscopic response for calibration and validation, experiments on microscopic observations are under investigation.

A. Elastic Properties

Anisotropic elastic constants of the hcp and bcc phases are evaluated by "fitting" the simulated elastic response of polycrystalline Ti-6242 to experimental data from the tension constant strain rate experiments. Details of the computational model for polycrystalline Ti-6242 are provided in Section VI. The components of the elastic stiffness tensor for the transversely isotropic hcp phase and the cubic symmetric bcc phase are presented in Table III. The components are measured in the material principal axes.

B. Crystal Plasticity Parameters

The flow and hardening parameters in the crystal-plasticity relations for the hcp and bcc phases in the transformed β single colonies are calibrated from corresponding mechanical test data. Initial estimates of the hcp phase parameters in these colonies are obtained from data on Ti-6Al single crystals obtained in the previous paper.[27] Finite element models of representative elements of the transformed β colonies are constructed for calibrating the bcc crystal parameters in transformed β regions. The models incorporate a unit cube discretized into 343-brick element C3D8 in ABAQUS/Standard (Figure 3). The models contain periodic morphological representation of the α and β laths in the lamellar structure. The α laths, occupying a volume fraction of 88 pct in the representative elements, have hcp crystal structure with 30 slip systems, whereas the β laths, with a 12 pct volume fraction, have a bcc crystal structure with 48 slip systems. To delineate the β lamella, two parallel planes that are equidistant from the centroid of the unit cube and normal to the e_2^c crystallographic direction of the hcp phase are drawn. The distance between the planes is adjusted iteratively to match the 12 pct β volume fraction. The β-crystal orientation is arranged to accommodate the Burger's relation between α and β phases. As shown in Figure 3(c), the $\alpha\beta$ interface and the β laths are uniquely oriented for activation of slip on each of the a_1, a_2, and a_3 basal and prismatic systems discussed in Sections III–A and III–B.

The microtensile and compression tests, discussed in Sections III–A and III–B, are simulated using the FEM model of each representative element corresponding to the maximum slip activity (corresponding to a Schmid factor of 0.5) on the a_1, a_2, and a_3 basal and prismatic slip systems. The simulations are conducted at a strain rate of 1.0×10^{-4} s^{-1} by applying a velocity field on the top face of the model to yield this rate. The bcc crystal-plasticity parameters calibrated by GA are m, $\dot{\tilde{\gamma}}$, g_0^α, h_0^β, h_s^β, τ_s^β and τ_0^β.

Tension-compression asymmetry of each slip system is accounted for in these calibrations. For example, the $<111>\{110\}$ system is symmetric with respect to the direction of shear along the $<111>$ axis, whereas the $<111>\{112\}$ and $<111>\{123\}$ are not. Slip in the latter two systems along one direction has a lower shear strength and higher energetic maximum than slip in the reverse direction.[39] Consequently, along each slip direction, a "hard direction" is designated that has a higher shear strength and energetic maximum compared to its reverse "soft direction." Crystal-plasticity parameters are calibrated separately for the hard and soft directions of the $<111>\{110\}$, $<111>\{112\}$, and $<111>\{123\}$ systems. The initial parameters for the hcp phase in the GA-based calibration are adopted from the Ti-6Al-4V results.[27] The calibration proceeds in two steps: (1) the flow parameters, which are first determined to match the yield point, and (2) the hardness evolution-related parameters, which are subsequently evaluated to match the hardening portion of the stress-strain curve. The corresponding single colony stress-plastic strain plots of experimental and computational results in the case of maximum activity on the hcp prismatic slip systems are shown in Figure 4. Crystal-plasticity parameters obtained by the calibration process are listed in Tables IV and V.

C. A Homogenized Crystal-Plasticity Model for the $\alpha + \beta$ Transformed β Phase

In the microstructure-based modeling of polycrystalline Ti-6242, it is computationally prohibitive to incorporate an
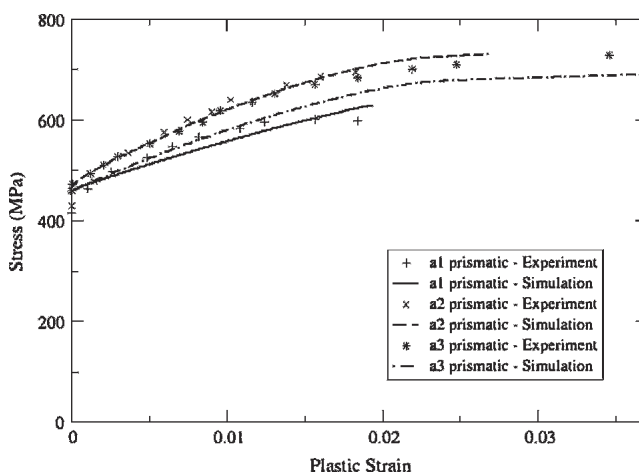

Fig. 4—Stress-strain plots for maximum slip along different prismatic systems in the transformed β single colonies, from experimental and FE simulation data.
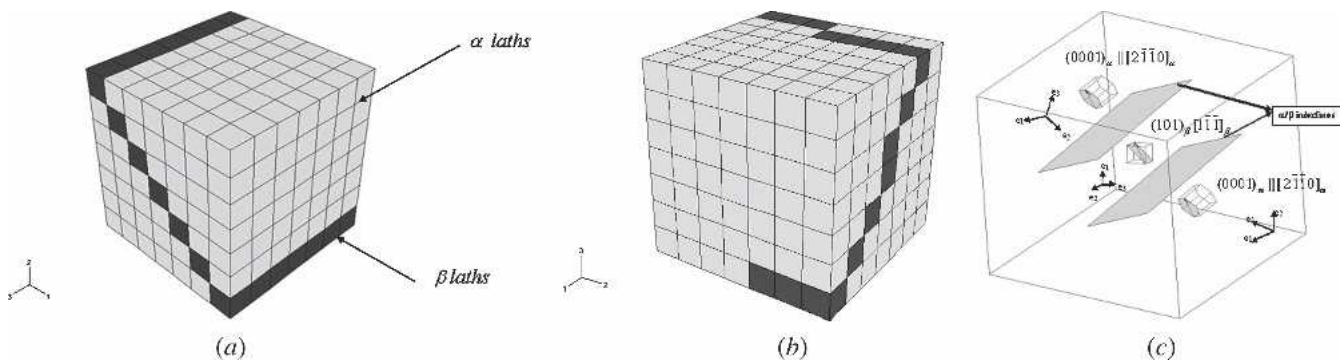

Fig. 3—FE model of representative elements of the transformed β single colonies consisting of parallel α and β laths for two different maximum slip activity orientations: (a) a_2 prismatic orientation, (b) a_3 basal orientation (dark regions [partially hidden] correspond to the β laths), and (c) schematic of the α/β interface and the β lath for an arbitrary hcp orientation showing the Burger's relation.

Table IV. Calibrated Parameters for the hcp Basal <a> and Prismatic <a> Slip Systems in the Transformed β Single Colonies From the Explicit Single-Colony Models

Parameters for Slip System	m	g_0 (MPa)	$\dot{\gamma}(s^{-1})$	h_0	r	$\widetilde{g}$ (MPa)	n
Basal<a>	0.02	300	0.0023	2000.0	0.3	504.0	0.14
Prismatic<a>	0.02	240	0.0023	4153.0	0.29	504.0	0.15

Table V. Calibrated Parameters for the bcc Slip Systems from the Explicit Single-Colony Models

Parameters for Slip System	m	g_0 (MPa)	$\dot{\gamma}(s^{-1})$	h_0	h_s	τ_0 (MPa)	τ_s (MPa)
{101}	0.02	250	0.0023	1500.0	25.0	500.0	200.0
{112} soft	0.02	209.63	0.0023	1979.8	25.0	500.0	200.0
{112} hard	0.02	229.82	0.0023	1371.6	25.0	500.0	200.0
{123} soft	0.02	200.67	0.0023	1634.8	25.0	500.0	200.0
{123} hard	0.02	251.28	0.0023	2312.0	25.0	500.0	200.0

Table VI. Constitutive Parameters for hcp Basal <a> and Prismatic <a> Slip Systems in Tension, Calibrated from the Equivalent Transformed β Model

Parameters for Slip System	m	g_0 (MPa)	$\dot{\gamma}(s^{-1})$	h_0	r	$\widetilde{g}$ (MPa)	n
a_1 basal	0.02	284	0.0023	1500.0	0.3	450.0	0.14
a_2 basal	0.02	315	0.0023	2300.0	0.3	634.0	0.1
a_3 basal	0.02	243	0.0023	8000.0	0.4	371.0	0.05
a_1 prismatic	0.02	240	0.0023	3450.0	0.29	504.0	0.15
a_2 prismatic	0.02	210	0.0023	6500.0	0.2	583.0	0.25
a_3 prismatic	0.02	240	0.0023	3600.0	0.3	504.0	0.15

explicit model of the transformed β colonies, as depicted in Figure 3. Consequently, a homogenized model of the $\alpha + \beta$ phase colony regions is developed for incorporation in the FE model of Ti-6242. The homogenized equivalent crystal consists of 78 slip systems, of which 30 correspond to hcp and 48 correspond to bcc slip systems. The bcc slip directions are aligned such that the Burger's relation $(101)_\beta \| (0001)_\alpha, [1\bar{1}\bar{1}]_\beta \| [2\bar{1}\bar{1}0]_\alpha.$ is enforced. Assumptions for a Taylor model are made in the construction of the equivalent crystal—i.e., a uniform deformation gradient F_{ij} is assumed for all phases in the transformed β colonies.[40] The second Piola-Kirchoff stress tensors $S_{ij}^{hcp}(F_{kl}, \dot{\gamma}_{hcp}^\alpha)$ and $S_{ij}^{bcc}(F_{kl}, \dot{\gamma}_{bcc}^\alpha)$ for the α and β phases are separately calculated from the 30 hcp and 48 bcc slip systems, respectively, using Eqs. [1] through [7] and the step integration previously discussed.[17,18] The corresponding true stress tensors in each of the phases are calculated by the transformation

$$\sigma_{ij}^{hcp}(F_{kl}, F_{mn}^{hcp(e)}) = \frac{1}{\det F_{mn}^{hcp(e)}} F_{ik}^{hcp(e)} S_{kl}^{hcp} F_{jl}^{hcp(e)} \text{ and}$$

$$\sigma_{ij}^{bcc}(F_{kl}, F_{mn}^{bcc(e)}) = \frac{1}{\det F_{mn}^{bcc(e)}} F_{ik}^{bcc(e)} S_{kl}^{bcc} F_{jl}^{bcc(e)} \quad [9]$$

where $F_{ij}^{hcp(e)}$ and $F_{ij}^{bcc(e)}$ are the elastic deformation gradients mentioned in Eq. [2]. Finally, the true stress tensor at the material point for the equivalent crystal is determined using the rule of mixtures, where a weighted averaging of the individual phase stresses is conducted, with phase volume fractions as weights. The corresponding stress is expressed as:

$$\sigma_{ij}^{tran-\beta} = \nu_f^{hcp}\sigma_{if}^{hcp}(F_{ij}, F_{kl}^{hcp*}) + \nu_f^{bcc}\sigma_{ij}^{bcc}(F_{ij}, F_{kl}^{bcc*}) \quad [10]$$

where ν_f^{hcp} and ν_f^{bcc} are the respective volume fractions. Since the volume fraction of the bcc phase in the transformed β colony is relatively small ($\sim$12 pct), the rule of mixtures-based model is deemed adequate. The equivalent transformed β-crystal model can be represented at each integration point of the finite element model with compactness and high efficiency, in comparison with the explicit models of Figure 3.

The constitutive parameters are re-examined for effectiveness with the equivalent model. The bcc parameters are kept the same as reported in Table V, calibrated with the explicit model. However, the hcp crystal-plasticity parameters are recalibrated using GA for concurrence with the experimental microtensile and compression data of Ti-6242 single colonies discussed in Sections IV–A and IV–B.[28] This data for constant strain rate tests at $\dot{\varepsilon} = 10^{-4}$ s^{-1} includes stress-strain plots for a_1, a_2, and a_3 basal and prismatic slip. In addition, the data also indicate a significant tension-compression asymmetry. The hcp parameters are consequently modified to calibrate different crystal-plasticity parameters $(m, \dot{\gamma}, g_0, h_0, r, \widetilde{g}, n)$. Tension-compression asymmetry is incorporated along the hcp slip systems using a criterion based on the sign of the maximum principal stress at a given point. For example, if this principal stress is positive, a set of constitutive parameters is associated with the slip system, whereas a different set of parameters is associated with a negative stress.

The resulting parameters are listed in Tables VI and VII. Excellent agreement between experimental and corresponding simulated stress-strain responses is seen in the plots of Figure 5. Furthermore, the accumulated shear strains on the bcc slip systems in the equivalent homogenized crystal model are compared with the average values of all slip systems for the explicit model of Figure 3. The slip system shear strains for basal and prismatic oriented simulations are tabulated in Table VIII corresponding to macroscopic strain of 0.024 in the loading direction. The dominant shear strains in each slip system are found to be good agreement for the two models. These tests provide validation for the equivalent crystal representation of the transformed β crystals.

VI. CRYSTALLOGRAPHIC ORIENTATION DISTRIBUTIONS IN THE FE MODEL

Each element in the FE representation of polycrystalline Ti-6242 aggregate, shown in Figure 6(c), represents a single globular α grain or $\alpha - \beta$ colony region. It is important to assign appropriate crystallographic orientation to the elements prior to FE simulation because deformation response is observed to be highly sensitive to the overall

Table VII. Constitutive Parameters for hcp Basal <a> Slip Systems in Compression, Calibrated from the Equivalent Transformed β Model

Parameters for Slip System	m	g_0 (MPa)	$\dot{\gamma}(s^{-1})$	h_O	r	$\widetilde{g}$ (MPa)	n
a_1 basal	0.02	388	0.0023	350.0	0.5	504.0	0.1
a_2 basal	0.02	450	0.0023	350.0	0.5	504.0	0.1
a_3 basal	0.02	455	0.0023	750.0	0.5	504.0	0.1

texture. The variants of crystallographic orientation distribution are studied in this paper and are discussed next. It must be emphasized that the orientation distributions (Euler angles) assigned with the methods developed represent hcp orientations only. The bcc orientations are calculated from the secondary hcp orientations using the Burger's orientation relation.

A. *Statistically Equivalent Orientation Distribution*

For physically meaningful simulations, crystallographic orientations that are statistically equivalent to those obtained from OIM techniques are assigned to the FE model. OIM involves electron back-scattered diffraction (EBSD) in scanning electron microscopy. A typical OIM map for the forged Ti-6242 sample showing the color-coded inverse pole figure [0001] produced by an EBSD scan with step size of 6 μm is shown in Figure 6(d). The statistically equivalent orientations are assigned using a orientation probability assignment method (OPAM) discussed previously.[16,41] In this method, crystallographic orientations, represented by Euler angles, are first generated from transformed pole figures, in which points in discretized regions of the projected plane are extracted from contour plots of the pole figures in X-ray diffraction analysis. This process generally generates a large number of Euler angles (14,799 in Figure 6(a)), considerably in excess of the assignable orientations to the FE model. Consequently, the OPAM assigns orientations with similar probability density distributions $f(g)$ of the crystallographic orientations to the finite element mesh, following a method discussed previously.[16,27] These steps in this process are: (1) An Euler angle space in an orthorhombic system is one in which the three coordinate axes are represented by three Euler angles (φ_1, Φ, φ_2; $0 \leq \varphi_1 \leq 360$ deg; $0 \leq \Phi \leq 90$ deg; $0 \leq \varphi_2 \leq 90$ deg) (2) A probability density function $f(g)\Delta g = \frac{\Delta V_g}{V}$ is defined as the probability of observing an orientation G in the interval $g \leq G \leq g + \Delta g$, where ΔV_g = the volume of crystals with orientations between g and $g + \Delta g$ and V = the total volume of all grains. Let $N^{(i)}$ be the number of points in the ith orientation space element ranging from (φ_1, Φ, φ_2) to ($\varphi_1 + \Delta\varphi_1$, $\Phi + \Delta\Phi$, $\varphi_2 + \Delta\varphi_2$) and N the total number of the orientation points in the reduced Euler angle space. Then, volume fraction of orientation can be expressed as
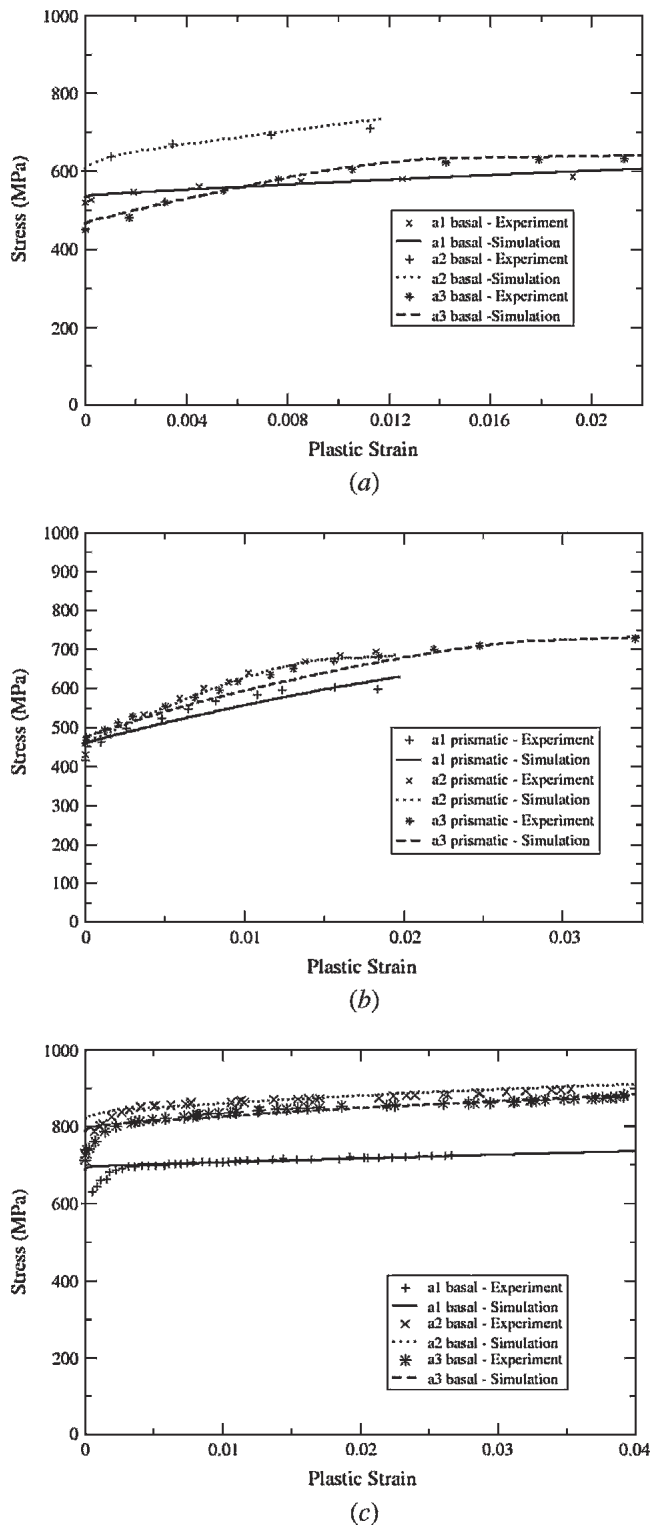
$$V_f^{(i)} = \frac{N^{(i)}}{N} \qquad [11]$$

Fig. 5—Experimental and simulation stress-strain plots using the equivalent model for maximum slip system activity on (*a*) basal tension, (*b*) prism tension, and (*c*) basal compressive slip systems.

(3) A orientation probability factor (P_i) for each orientation space element is obtained as

$$P_i = KV_f^{(i)} \qquad [12]$$

where K = a number that is equal to or larger than the number of orientations to be assigned to the finite element mesh. The complete set of statistically equivalent orientations is then $P = \sum_{i=1}^{n} P_i$, where P is equal to or larger than the number of grains in the finite element model, (4) Q ($\leq P$) sets of Euler angles are randomly selected from the orientation population P and are assigned to the integration points of different grains in the computational model.

Experimentally measured (0001) pole figures with 14,799 orientations are compared with 2744 simulated orientations assigned by OPAM in Figures 6(a) and (b). The convergence of the OPAM algorithm has been tested by increasing the number of elements in the FEM model. While larger number of elements yield better concurrence, the number of elements is optimally kept to a low value for efficient crystal-plasticity calculations. All textures are adequately represented in the simulated model. Convergence of the OPAM is also shown with the Rodrigues vector representation[42] in Figure 7 for the experimental and simulated crystallographic orientations. For better contrast, a logarithmic plot of the Rodrigues vector density is shown in this figure.

B. Statistically Equivalent Misorientation and Orientation Distribution

Computational studies have shown[16] that large stresses and plastic strain concentrations can arise at grain boundaries that exhibit large values of misorientation with their neighbors. Consequently, the second microstructural variant in the FE model creates a statistically equivalent misorientation distribution (MOD), in addition to the orientation distribution. The misorientations in this study are limited to the first neighbors of a grain only. The misorientation between two neighboring grains A and B is measured in terms of a rotation axis vector **n** and a misorientation angle θ, as described previously.[16] The axis **n** represents a common crystallographic lattice or slip direction for both crystal lattices. The angle θ is the rotation about **n** required to bring the two crystal lattices into coincidence. The misorientation angle θ between two neighboring grains is expressed quantitatively as:[43]

$$\theta = \min \left| \cos^{-1} \left\{ \frac{\mathrm{tr}(\boldsymbol{g}_A \boldsymbol{g}_B^{-1} \mathbf{O} - 1)}{2} \right\} \right| \qquad [13]$$

where $\boldsymbol{g}_A$ and $\boldsymbol{g}_B$ = the orientation matrices of grain A and B, respectively, and **O** is the crystal symmetry operator. Considering that there are 12 identical rotation operations in hexagonal symmetry, the misorientation of the two lattices can be described by 12 different symmetrically equivalent rotations. The minimum rotation angle is chosen as the misorientation angle. The method of producing equivalent MOD in the simulated microstructure, starting from that with an equivalent orientation only, is termed the misorientation probability assignment method (MPAM). Steps invoked in MPAM are as follows: (1) A set of 18 misorientation bins is created for misorientation angles between 0 and 90 deg. Each bin in this set has an angle increment of 5 deg, (2) The experimental data of misorientation angles between immediate neighboring grains is recorded. The number of grain pairs, for which the misorientation angle is within each of the 5-deg angular increments, is recorded. The average number fraction of grain-pairs per unit misorientation angle is plotted in Figure 8(a), and (3) Simulation of the FEM mesh and model starts with a calculation of

Table VIII. Comparison of Shear Strain Values on Prominent bcc Slip Systems (Highest Value of Shear Strain) for Different Orientations

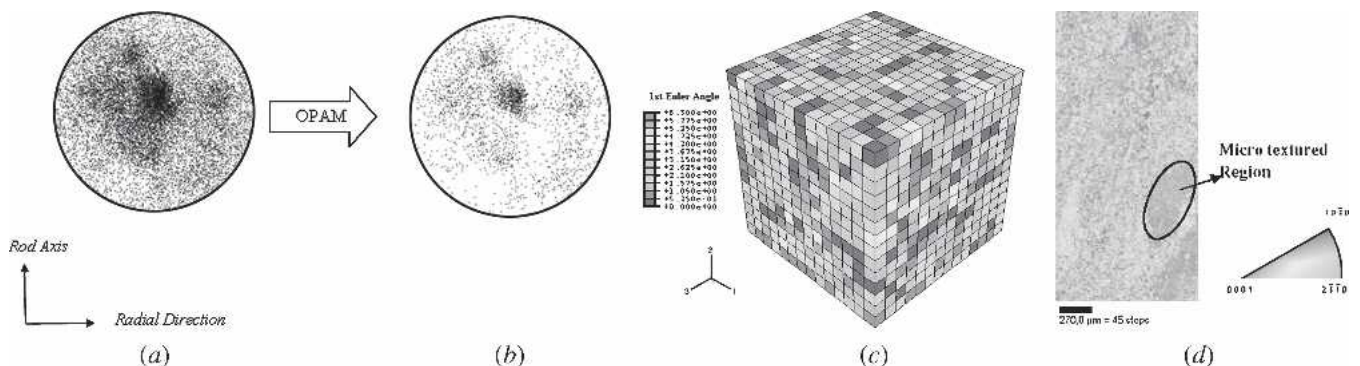| Orientation	BCC Slip System	Strain in Explicit Model	Strain in Equivalent Model
$\mathbf{a}_1$ basal	$[\bar{1}\,1\,1](1\,0\,1)$	3.22e-2	3.5e-2
	$[1\,1\,1](2\,1\,\bar{3})$	7.47e-3	4.38e-2
$\mathbf{a}_2$ basal	$[1\,1\,\bar{1}](1\,1\,2)$	2.19e-2	9.11e-3
	$[1\,1\,\bar{1}](1\,0\,1)$	2.10e-2	2.23e-2
$\mathbf{a}_3$ basal	$[1\,1\,\bar{1}](1\,0\,1)$	2.13e-2	2.57e-2
	$[1\,1\,1](\bar{3}\,1\,2)$	1.44e-2	1.01e-2
$\mathbf{a}_1$ prismatic	$[\bar{1}\,1\,1](1\,2\,\bar{1})$	3.8e-2	3.85e-2
	$[1\,1\,1](\bar{2}\,3\,1)$	2.06e-3	1.8e-3
$\mathbf{a}_2$ prismatic	$[1\,\bar{1}\,1](3\,1\,\bar{2})$	1.13e-2	2.5e-2
	$[1\,1\,1](\bar{3}\,1\,2)$	6.5e-3	1.89e-2
$\mathbf{a}_3$ prismatic	$[1\,1\,\bar{1}](\bar{1}\,3\,2)$	1.69e-2	1.5e-2
	$[1\,1\,\bar{1}](\bar{2}\,3\,1)$	1.68e-2	1.64e-2

Fig. 6—Orientation assignment to the finite element mesh: (a) experimentally observed (0001) inverse pole figure with 14,799 points, (b) OPAM simulated inverse pole figure with 2744 points, (c) FE model showing element orientations; the color represents the first Euler angle of the grain in radians, (d) OIM image showing the color-coded inverse pole figure [0001] produced by EBSD scan with step size of 6 μm. The clustering of similarly shaded regions displays the significant amount of microtexturing in the sample.
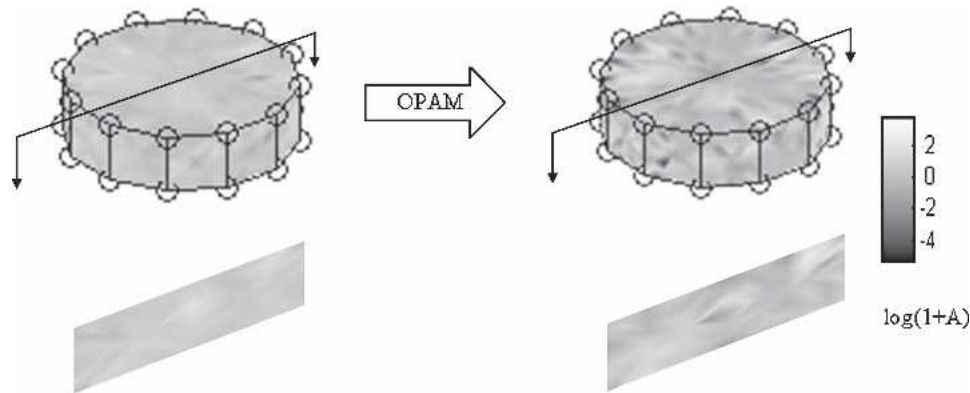
Fig. 7—Comparison of crystallographic texture using Rodrigues space representation together with a section showing the interior strength (*a*) from OIM and (*b*) from OPAM-based simulations. *A* is the density of Rodrigues vector points.
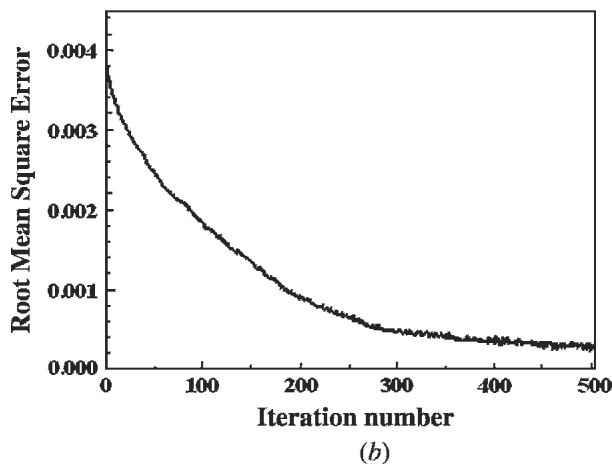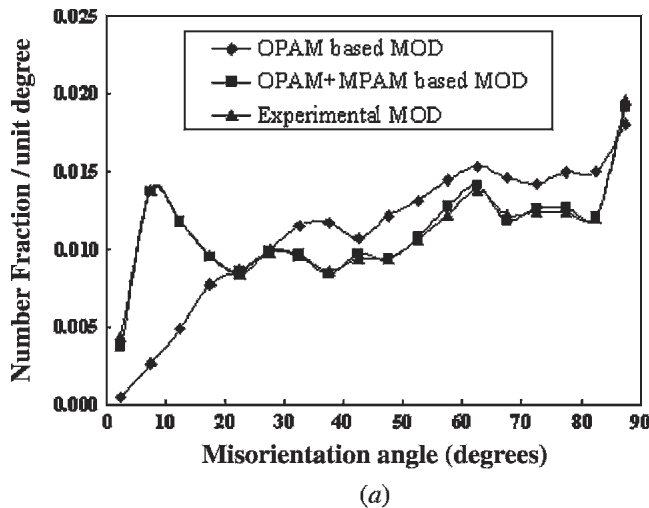

(*a*)

(*b*)

Fig. 8—(*a*) Comparison of the volume fraction per unit angle as a function of the misorientation distribution (MOD) for OIM-generated experimental data, and simulated data generated by (i) the OPAM algorithm alone and (ii) the OPAM + MPAM algorithm; and (*b*) convergence plot of RMS error with increasing iterations, showing the convergence of the MPAM algorithm.

the misorientation angle θ_o for the model with statistically equivalent orientation distribution by OPAM alone. The corresponding starting average number fraction per unit angle is plotted in Figure 8(a). The poor match in MOD with the

experimental plot is evident from this figure, (4) The 18 statistical bins are rank-ordered based on the difference in their number fraction values between the experimental and simulated misorientation distributions. The bin with the largest difference value is assigned the greatest rank. The rank is also given a sign to signify whether it is in excess or deficit over the experimental bin. The excessive bins receive a positive sign and the deficient bins are ranked with a negative value, (5) For every element *i* and its neighbor *j* in the FE model, the misorientation angle is designated as θ_{ij}, and $R(\theta_{ij})$ corresponds to the rank of the bin to which θ_{ij} belongs. An element acceptability index $EAI_i = \sum_{j=1}^{n} R(\theta_{ij})$ is calculated as the sum of the ranks of the misorientation bins to which a given element contributes. Elements with the highest EAI_i are the least acceptable elements and are moved around in the FE mesh to reduce this value, and (6) This process of successive iteration is continued until an acceptable MOD match is reached. In every iteration, a root mean square (RMS) error of the simulated mesh, $\sqrt{\sum_{i=1}^{9} (e_i - s_i)^2}$, is calculated. Here e_i and $s_i =$ the number fraction of grains in each bin for the experimental and simulated MODs, respectively.

The final MOD obtained from 500 iterations of the OPAM + MPAM method discussed above is shown in Figure 8(a). The rate of convergence of the method with respect to the RMS error is demonstrated in Figure 8(b).

C. *Equivalent Misorientation Distribution and Assignment of Microtexture*

The orientation and misorientation assignment (OPAM + MPAM) method discussed above does not guarantee spatial arrangement of the grains in the model to form the contiguities or microtextures that are observed in the OIM maps (*e.g.,* in Figure 6(d)). Woodfield *et al.*[44] have observed that specimens of α/β processed Ti-6242 that contain large microtextured regions of primary α colonies have a significantly shorter life than those with no predominant microtexturing. Additionally, the microtextured specimens show faceted fatigue crack initiation.[44] This motivates a statistically equivalent representation of the microtexture, observed in OIM maps of

the Ti-6242 microstructure in Figure 6(d), in the FE model. As in Section VI–B, an iteration method is used to match the microtexture using a microtexture probability assignment method (MTPAM), with the following steps: (1) A set of four statistical bins is set up for number fraction of grains that have low misorientations with their neighbors (<15 deg). The bins are for the cases when (1) almost none of the neighbors have a low misorientation, (2) between 0 and 33.33 pct of the neighbors have a low misorientation, (3) between 33.33 pct and 66.66 pct of neighbors have a low misorientation, and (4) between 66.66 pct and all of the neighbors have a low misorientation. A histogram of the experimental microtexture is shown in Figure 9(a). The importance of the last bin that has similarly oriented regions is high in the algorithm for determining microtexture and needs to be represented with a higher weight (2) Every element i is assigned a value, n_i^p that corresponds to the number of its neighbors with which it has a low misorientation. For cubic elements in this work, the number can vary between 0 and 6. Elements (i) at the core are referenced as primary and its neighbors (j) are termed as secondary. Each secondary element is assigned a value n_{ij}^s of either zero or the n_i^p value of the primary element, depending of whether the misorientation is low (<15 deg in this case) or otherwise. For example, if a primary element i has a low misorientation with five of its six neighbors, then $n_i^p = 5$. Correspondingly, $n_{lm}^s = 0$ for all the five secondary elements, and the sixth neighbor is assigned a $n_{lm}^s = 5$ (3) After completing the value assignment process for every element in the ensemble, the n_{ij}^s values for an element (one from each neighbor) are summed. The final value assigned to an element i is termed its *cluster contribution rating* (CCR_i) and is given as

$$CCR_i = \sum_{j=1}^{n} n_{ij}^s \hat{f}(\theta_{ij}) \text{ no sum on } i \qquad [14]$$

where $\hat{f}(\theta_{ij}) \begin{cases} 1 \forall \theta_{ij} \leq 15° \\ 1 \forall \theta_{ij} > 15° \end{cases}$ and n = the number of neighbors of element i. The grains with the highest CCR_i are considered least acceptable and are selected for relocation. Experimental and initial (generated by OPAM + MPAM) histograms of the number fraction of grains *versus* the fraction of their neighbors having a low misorientation (<15 deg) are shown in Figures 9(a) and (b). Figure 9(c) shows the final distribution of fraction of neighbors with low misorientation after the microtexture has been matched using the MTPAM algorithm. To test the convergence rate of the MTPAM algorithm, a weighted RMS error $\sqrt{\sum_i w_i (e_i - s_i)^2}$ is evaluated at every step. The weights w_i are determined according to their relative importance in the determination of microtexture. For example, weights of 0.25, 0.5, 0.75, and 1.0 are assigned for the first, second, third, and fourth bins from the left, respectively. Figure 9(d) is a plot of the weighted RMS error as a function of progressive iterations in the MTPAM algorithm, exhibiting the rate of convergence of the algorithm.
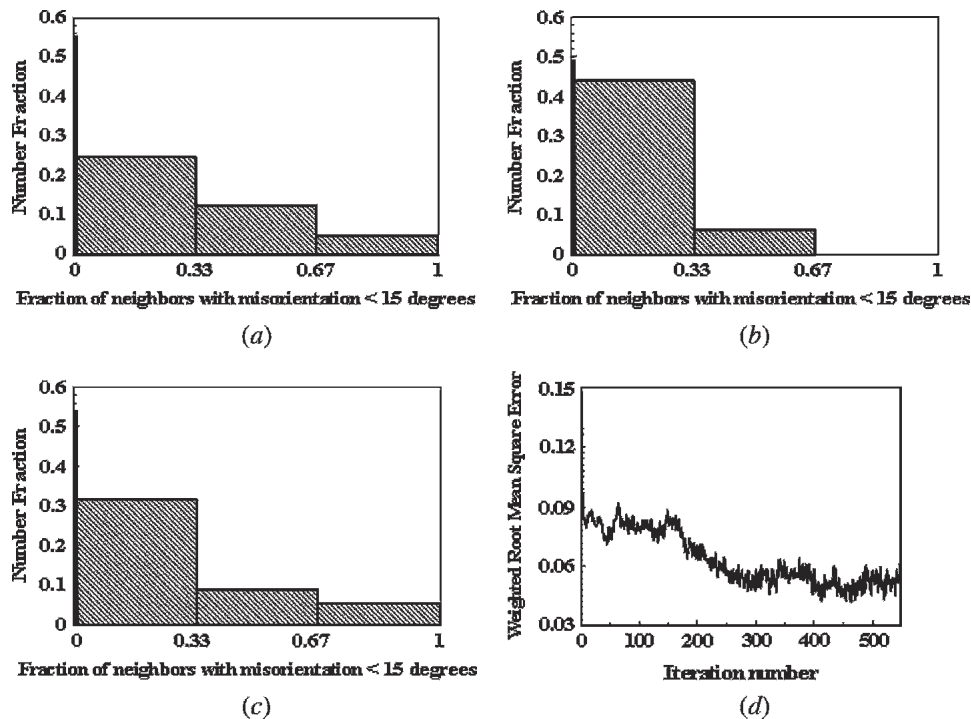

Fig. 9—Histograms of the number fraction of grains as a function of the fraction of their neighbors having a low misorientation (<15 deg), corresponding to (a) experimental microtexture from OIM, (b) simulated initial microtexture with OPAM + MPAM alone, (c) simulated final microtexture with MTPAM, and (d) convergence plot of weighted RMS error with increasing iterations.

VII. VALIDATION OF THE TI-6242 MODEL FOR CONSTANT STRAIN RATE AND CREEP TESTS

The computational model developed for polycrystalline Ti-6242 alloy is now validated with experimental results described in Section IV. Simulations of two types of mechanical tests (constant strain rate tests and creep tests) are conducted both for tension and compression. The imposed strain rate for both compression and tension tests is 1×10^{-4} s^{-1}. For the creep tests, the compression test is conducted at 95.5 pct of the yield stress or 907 MPa, whereas the tension test is at 94.4 pct of the yield stress (897 MPa). The experiments exhibit considerable tension-compression asymmetry for Ti-6242 alloy, with stronger macroscopic response in compression than in tension. Also, the creep strain accumulation is found to follow a power law behavior in time, with monotonically decreasing creep rates.

A. The FE Model with Boundary Conditions

The FE ensemble model of the polycrystalline aggregate consists of a unit cubic domain that is discretized into 2744 eight-noded brick elements in ABAQUS (C3D8). Each element in the FE model represents a grain, and the distribution of these elements is assigned to conform to the three variants as described in Section VI. The total number of grains in the model is found to project a convergent behavior with respect to macroscopic response—*i.e.,* adding grains do not change the response. Seventy percent of the grains are primary α that have hcp crystal structure, and the remaining 30 pct are transformed β grains represented by the homogenized equivalent model of Section V–C.

All rigid body modes of the computational model are suppressed. To simulate the constant strain rate tests, a displacement boundary condition is applied to the top face of the unit cube as

$$l_o(\exp(\dot{\varepsilon}_c t) - 1) \qquad [15]$$

where l_o = the initial dimension (=1) of the cube and $\dot{\varepsilon}_c$ is the applied strain rate. To simulate the creep experiments, a uniform pressure boundary condition, ramped from zero to the desired creep load in an interval of 0.0084 seconds, is applied to the top face using the DLOAD routine of ABAQUS.

B. Modified Material Parameters Accounting for Size Effects

The α/β laths in the transformed β phase of the polycrystalline Ti-6242 are much finer than the single-colony samples used in the calibration process of Section V. Also, the primary α grains in Ti-6242 are smaller than those in the calibrated single-colony regions previously investigated.[27] Strengthening with smaller lath size in β processed Ti-6Al-4V has been experimentally observed,[45] and the same effects prevail in Ti-6242, making the *in situ* phases relatively stronger. Consequently, crystal-plasticity parameters calibrated from single-crystal and single-colony tests should be modified for incorporating the Hall-Petch or size effects prior to their use in the polycrystalline models. While strain gradient-based models developed for the size effect[46,47,48] are no doubt more accurate and are in development, an initial size dependence through parameter scaling is implemented for its simplicity in this work.

The effect is incorporated by increasing the initial slip system deformation resistance g_o^γ by a factor χ. For the secondary α in the transformed β colonies, the factor χ for individual slip systems is evaluated from polycrystalline constant strain rate results in tension and compression. The corresponding modified g_o^γ and χ values are reported in Table IX. Other calibrated values of g_o^γ, for which direct experimental data are not available, include 450 MPa for the prismatic compression test, 640 MPa for the <c + a> pyramidal tension test, and 802 MPa for the <c + a> pyramidal compression test. These values yield a good fit for the polycrystalline constant strain rate tests. The adjusted values of the β phase (bcc) in the colonies are also documented in Table IX. For the equiaxed primary α phase, the g_o^α values are best estimated by the a_1-type slip systems of the secondary α regions because of the easy slip transmission through the α/β lamellar boundary. Also due to the absence of any β phase, the three <a>-type slip vectors are not unique in the primary α regions, and equal parameters are assigned to all of them. The values of g_o^γ for the primary α regions are modified over those previously determined[27] for α-Ti-6Al and are listed in Table X. The corresponding hardness evolution-related parameters are given in Table XI to obtain good fits for the constant strain rate tests.

Table IX. Modified Values of the Initial Deformation Resistance g_o^γ for Secondary α (hcp) and β (bcc) Laths in Transformed β Regions due to Finer Lath Sizes Compared to Single-Colony Structure

Tensile (secondary α)						
Parameter	a_1 basal	a_2 basal	a_3 basal	a_1 prismatic	a_2 prismatic	a_3 prismatic
Modified g_o^α	430 MPa	440 MPa	400 MPa	390 MPa	380 MPa	400 MPa
χ	1.51	1.4	1.65	1.625	1.81	1.67
Compressive (secondary α)						
Parameter		a_1 basal		a_2 basal		a_3 basal
Modified		460 MPa		490 MPa		480 MPa
χ		1.19		1.09		1.06
β phase						
Parameter	{101}	{112} soft	{112} hard	{123} soft		{123} hard
Modified	450 MPa	409.63 MPa	429.82 MPa	400.67 MPa		451.28 MPa
χ	1.8	1.95	1.87	2.00		1.79

Table X. Modified Values of the Initial Deformation Resistance g_o^γ for Primary α Grains to Account for Size Effects

	Basal <a> System	Prismatic <a> System	Pyramidal <c + a> System
Tensile	385 MPa	365 MPa	640 MPa
Compressive	430 MPa	465 MPa	760 MPa

Table XI. Hardness Evolution-Related Parameters for the Primary α Region

Parameters for Slip System	h_0	r	$\tilde{g}$ (MPa)	n
Basal <a>	100.0	0.1	450.0	0.01
Prismatic <a>	100.0	0.1	550.0	0.01
Pyramidal <c + a>	100.0	0.1	1650.0	0.01

C. *Results of the Validation Simulations*

The average stress-strain responses for the constant strain rate tests are plotted in Figures 10(a) and (b) and compared with experimental results. The stresses and strains are in the direction of the applied displacement (X_2), for which the volumetric averages are defined as

$$\bar{\sigma}_{22} = \frac{\sum_{i=1}^{nel}\sum_{j=1}^{npt}(\sigma_{22}J)_{ij}}{\sum_{i=1}^{nel}\sum_{j=1}^{npt}(J)_{ij}}, \quad \bar{\varepsilon}_{22} = \frac{\sum_{i=1}^{nel}\sum_{j=1}^{npt}(\varepsilon_{22}J)_{ij}}{\sum_{i=1}^{nel}\sum_{j=1}^{npt}(J)_{ij}} \quad [16]$$

$(\sigma_n^\tau)$where σ_{22} and δ_{22} = the Cauchy stress and the total strain at each element integration point and J = the determinant of the Jacobian matrix at these integration points. The total number of elements in the model is *nel* and *npt* corresponds to the number of integration points per element.

Figure 10(a) shows the comparison for the tensile constant strain rate test, whereas Figure 10(b) shows that for the compression test. The FE model is able to capture the behavior of polycrystalline Ti-6242 rather well, even with a very limited number of experiments for material property calibration.For the creep tests, the volume-averaged plastic strains are plotted as functions of time in Figure 11 and compared with experiments. Figures 11(a) and (b) are for responses in compression and tension creep tests, respectively, over a very long period of time. Considering variabilities in the model and the range of time over which the experiments are conducted, the agreement between the experimental and simulated results is quite good. The strain rate decreases by orders of magnitude during the duration of these creep tests and roughly follows a power law response with time. These characteristics are also accurately reproduced by the model.

VIII. GRAIN-LEVEL PREDICTIONS OF STRESSES AND STRAINS

The validated computational model for Ti-6242 is now used to understand the effect of the local microstructure on
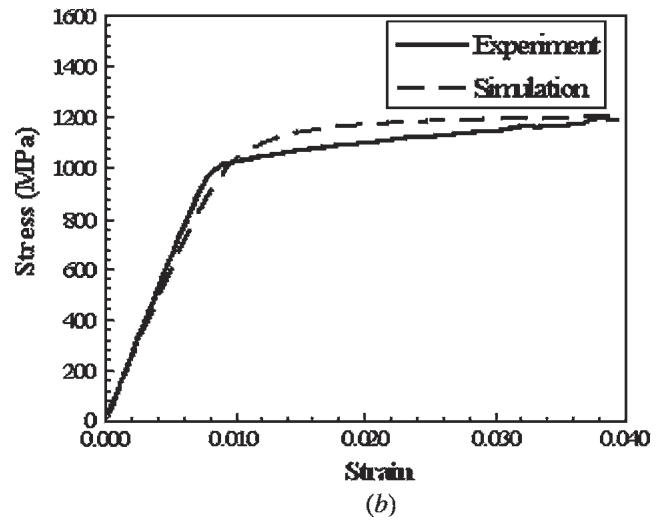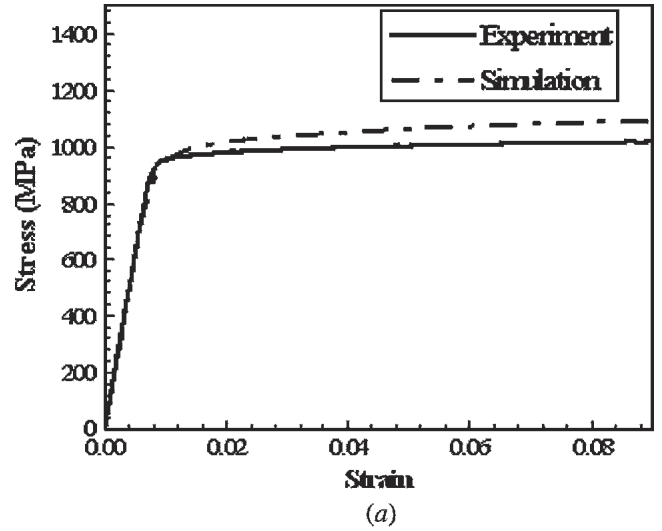

Fig. 10—Validation of the Ti-6242 computational model with experimental results for constant strain rate test: (*a*) tensile at a strain rate = 1.0×10^{-4} s^{-1} and (*b*) compressive at a strain rate = 1.0×10^{-4} s^{-1}.

the local stress and strain evolution. Two studies are undertaken with respect to this overall objective.

A. *Local Evolution of Stresses and Plastic Strain with Time and Load-Shedding Effects*

Woodfield *et al.*[44] have observed in their dwell fatigue experiments on α/β processed Ti-6242 that α grains always crack at or close to the basal plane. Bache *et al.*[46] have mentioned that grains in $\alpha + \beta$ Ti alloys with their basal planes nearly perpendicular to the principal stress axis act as strong regions and promote the formation of cleavage facets with a near-basal plane orientation. Stress redistribution between microstructural regions with different strengths has been proposed as the fundamental cause of the development of these faceted cracks. In the present paper, the stress normal to the basal plane $(\sigma_n^\tau)$of α grains is studied as a critical variable likely to cause crack initiation. Orientations unfavorable for easy <**a**>-type slip and local load shedding from neighboring softer grains produce high local σ_n^τ in some grains, and these act as potential sites of crack initiation.
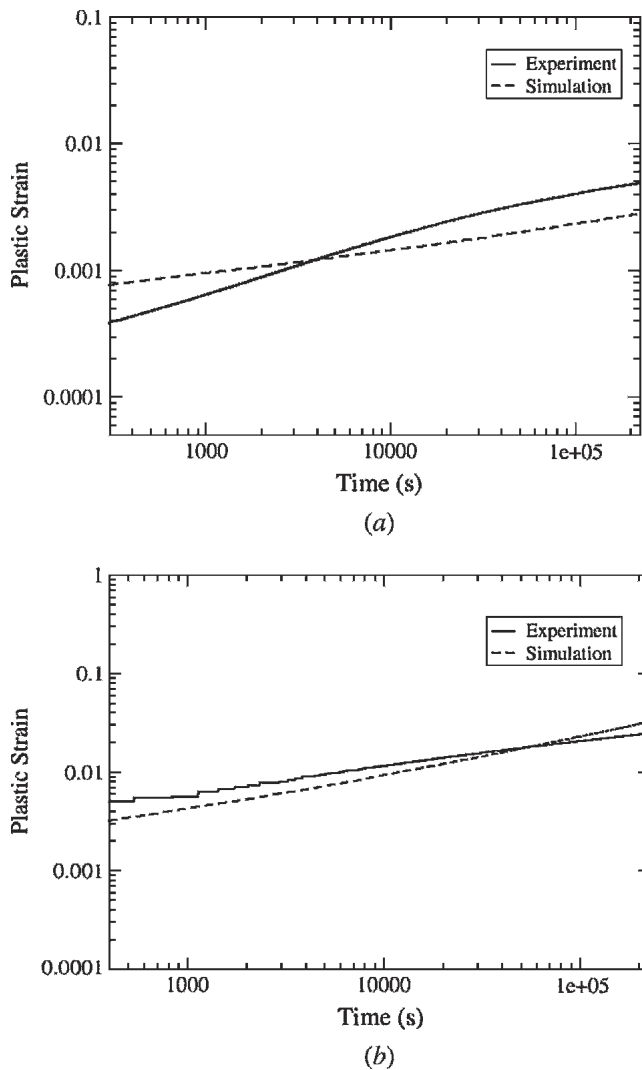
(a)

(b)

Fig. 11—Log-log plot of creep strain variation with time creep showing the experimental and the simulation results for stress levels of (*a*) 907 MPa in compression and (*b*) 897 MPa in tension.

To study this phenomenon, the polycrystalline model consisting of 2744 elements is simulated for compressive creep with a load of 907 MPa applied to its top face for 225,000 seconds. All Ti-6242 polycrystalline simulations are done with the statistically equivalent microtexture generated by OPAM + MPAM + MTPAM described in Section VI. The component of the stress vector $\boldsymbol{\sigma}_n^{\tau}$ along the [0001] axis of the hcp crystal is expressed as

$$\boldsymbol{\sigma}\frac{\tau}{n} = n_{\tau}(\boldsymbol{\sigma}\mathbf{n}_{\tau}) \qquad [17]$$

where $\mathbf{n}_{\tau}$ = the direction cosines of the [0001] axis in the global coordinate system at a time τ. It is calculated as:

$$\mathbf{n}_{\tau} = \mathbf{F}^{e^{-T}}(\boldsymbol{\tau})\mathbf{n}_0 \qquad [18]$$

where $\mathbf{n}_0$ is the initial orientation of the [0001] axis. The time evolution of microscopic variables along different sec-

tion through the polycrystalline microstructural cube shown in Figures 12 through 16.

Figure 12(a) is a plot of the evolving $\boldsymbol{\sigma}_n^{\tau}$ along a test line 1 to 1′ in the *x*-direction, which passes through the highest stressed grain. The distribution of $\boldsymbol{\sigma}_n^{\tau}$ is very nonuniform across 1 to 1′ owing to strength mismatches in the heterogeneous microstructure. The local stress in certain regions rises with time as a consequence of creep. This results in the local phenomenon of load shedding, where neighboring grains with large orientation mismatches see a significant rise in stress gradients across the interface. Even though the applied stress is 907 MPa, the highest value of σ_n^{τ} reached with time is more than 1200 MPa at point A in Figure 12(a). This corresponds to a grain for which the [0001] crystal axis makes an angle of 5.25 deg with the loading axis (*i.e.*, θ_c = 5.25 deg). The low θ_c results in high <**c** + **a**> activity. Because the critical resolved shear stress along the <**c** + **a**> slip systems is higher than the <**a**>-type slip systems, the grain exhibits a high value of σ_n^{τ}. Also, this grain has a high degree of misorientation with its neighbors, with an average misorientation θ_{av_mis} = 43.72 deg and a maximum misorientation θ_{max_mis} = 63.1 deg. This intensifies high stresses in the grain due to load shedding of the neighboring softer grains. The point B in Figure 12(a) depicts a typical grain with low $\boldsymbol{\sigma}_n^{\tau}$. For this grain θ_c = 88.33 deg, which has the effect of producing a nearly zero resolved stress along the [0001] axis on the basal plane. While the local stresses also increase with time, the rise is not significant from 6 seconds to 225,000 seconds. This is because of a small value of the strain rate exponent m = 0.02.

The evolution of the loading direction stress is shown in Figure 12(b). The load-shedding effects are even more prominent in this plot. The grain represented by point B sheds load onto the grain represented by point A with the passage of time. Figure 12(c) is a plot of the plastic strain in the loading direction along the line 1 to 1′. At t = 6 seconds, the creep load has stabilized and small levels of plasticity develop in local regions of the microstructure. At t = 225,000 seconds, the plastic strain has increased considerably because of creep and is nonuniformly distributed across A–A due to strength mismatches. Point A on the plot of Figure 12(c) corresponds to the grain with the highest $\boldsymbol{\sigma}_n^{\tau}$ of Figure 12(a), where low plastic strain is observed owing to the grain's high strength.

Figure 13(a) is a plot of evolving $\boldsymbol{\sigma}_n^{\tau}$ along a line 2 to 2′, parallel to the *x*-axis that lies on the top surface of the computational model (see Figure 12(a)). Among all grains that lie on 2 to 2′, the lowest angle made by the [0001] axis with the loading axis is θ_c = 38.0 deg. This corresponds to point A on the plot, where the highest $\boldsymbol{\sigma}_n^{\tau}$ occurs. Figure 13(b) is a plot of the corresponding plastic strain in the loading direction along 2 to 2′. The basal normal stresses along a line 3 to 3′ passing through the center of the computational cube is plotted in Figure 14(a). Point A, representing the highest stressed grain, has values of θ_c = 4.42 deg, θ_{max_mis} = 84.31 deg, and θ_{av_mis} = 56.62 deg. Points B, C, and D have θ_c = 61.83 deg, 78.14 deg, and 74.38 deg, respectively, and therefore exhibit a low value of $\boldsymbol{\sigma}_n^{\tau}$. Figure 14(b) shows the evolution of plastic strain along 3 to 3′, where point A has a low value of plastic strain owing to low <**a**>-type
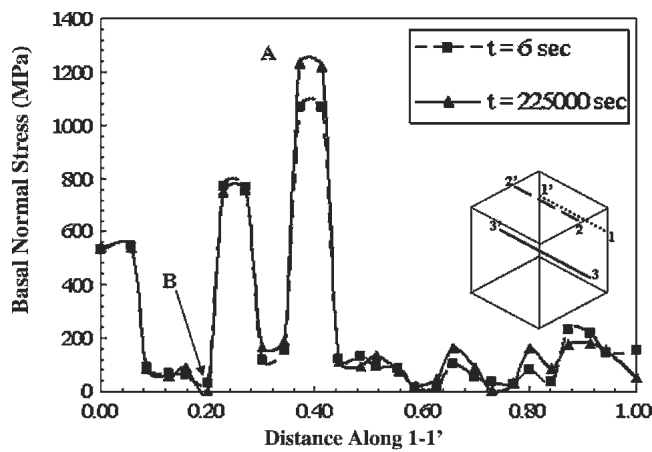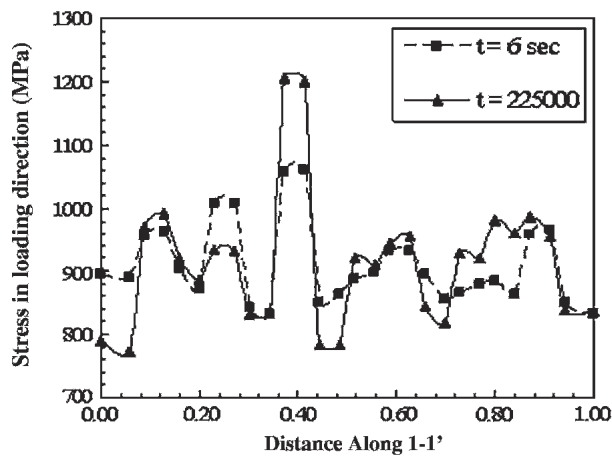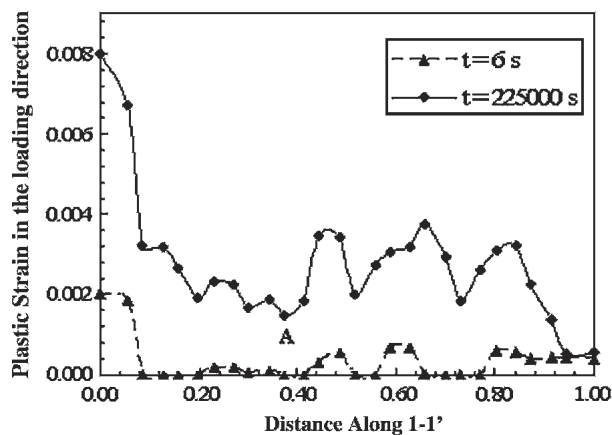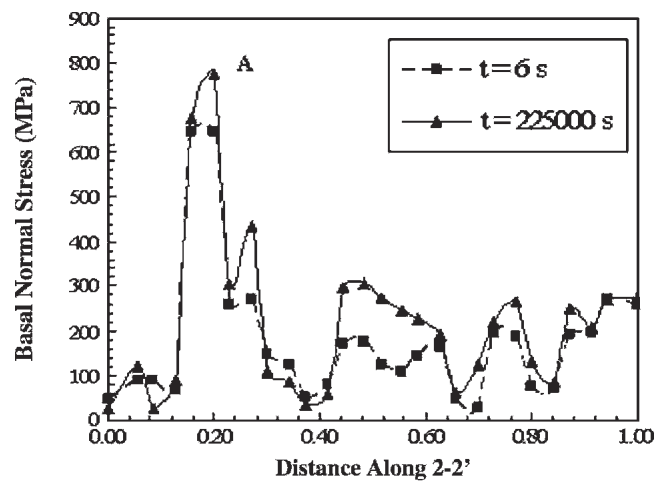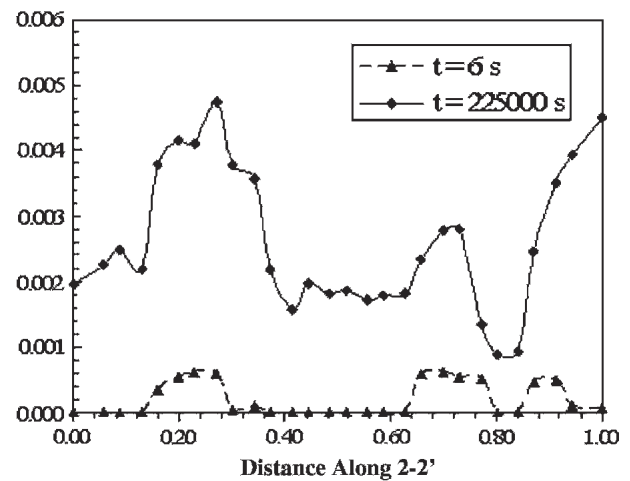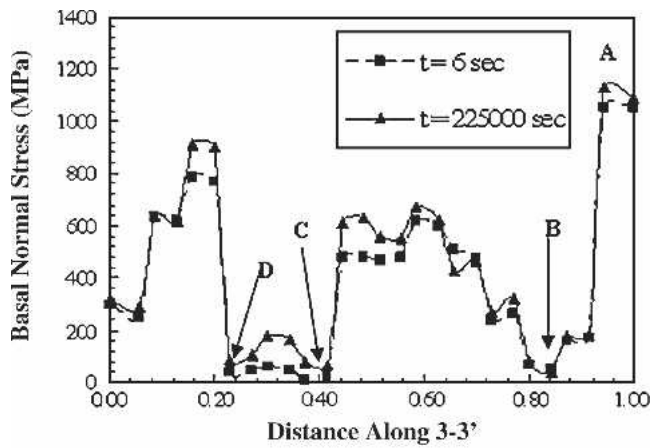
Fig. 12—Time evolution of microscopic variables along a section 1 to 1'
in the polycrystalline microstructure showing load-shedding behavior: (a)
basal normal stress, (b) stress in the loading direction, and (c) equivalent
plastic strain variation. Line 1 to 1' (see inset of (a)) is parallel to the x-axis
through the maximum stressed element in a computational unit cube.

Fig. 13—Time evolution of microscopic variables along a section 2 to 2'
in the polycrystalline microstructure showing load-shedding behavior: (a)
basal normal stress and (b) plastic strain. Line 2 to 2' is parallel to the x-axis
on the top face of the computational unit cube model.

slip activity. Similar behavior has also been noticed for tension creep, which will be reported in an upcoming paper.

A comparison of σ_n^{τ} for three representative grains is made in Figure 15. Grain 1 has a high $\theta_c = 74.17$ deg

and exhibits low misorientation with its neighbors, having values of $\theta_{max\_mis} = 62.82$ deg and $\theta_{av\_mis} = 20.26$ deg. In fact, grain 1 is a part of a colony of similarly oriented α grains. Grain 2 has the values $\theta_c = 6.16$ deg, $\theta_{max\_mis} = 80.3$ deg, and $\theta_{av\_mis} = 46.59$ deg. Grain 3 is less $<c + a>$ oriented than grain 2 but exhibits higher misorientation with its neighbors, with values of $\theta_c = 13.83$ deg, $\theta_{max\_mis} = 90.99$ deg, and $\theta_{av\_mis} = 62.82$ deg. σ_n^{τ} of grain 3 is observed to be higher than that of grain 2 even though the θ_c of the former is higher. This observation points to the importance of high stresses caused by high misorientation in the local material response, necessitating the representation of accurate MOD in the FE model. As can be expected, σ_n^{τ} values of grain 2 and 3 far exceed that of grain 1.

B. *Effect of Different Orientation Distributions and Microtextures*

The evolution of macroscopic and microscopic stresses and strains is analyzed for the three variants of the simulated microstructure discussed in Section VI. The textures
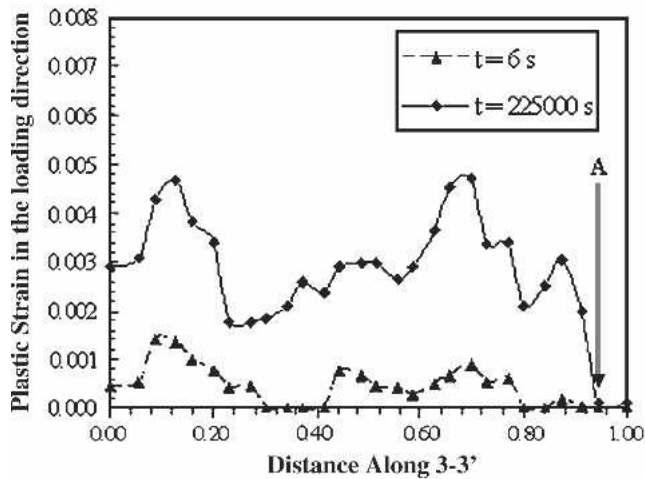
Fig. 14—Time evolution of microscopic variables along a section 3 to 3' in the polycrystalline microstructure showing load-shedding behavior: (a) basal normal stress and (b) plastic strain variation. Line 3 to 3' is parallel to the x-axis and passes through the center of the computational unit cube.
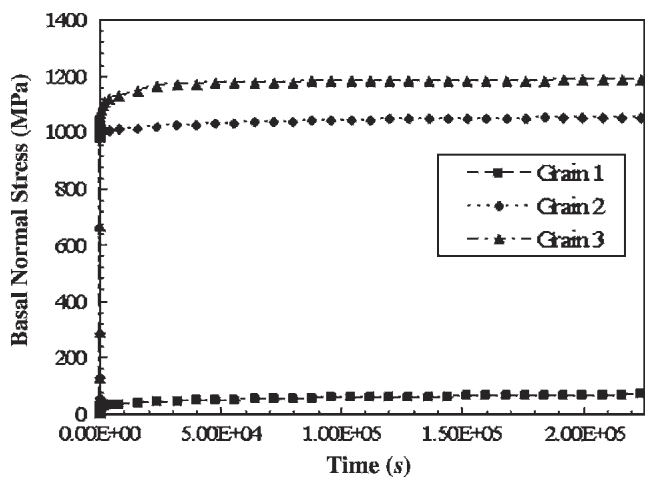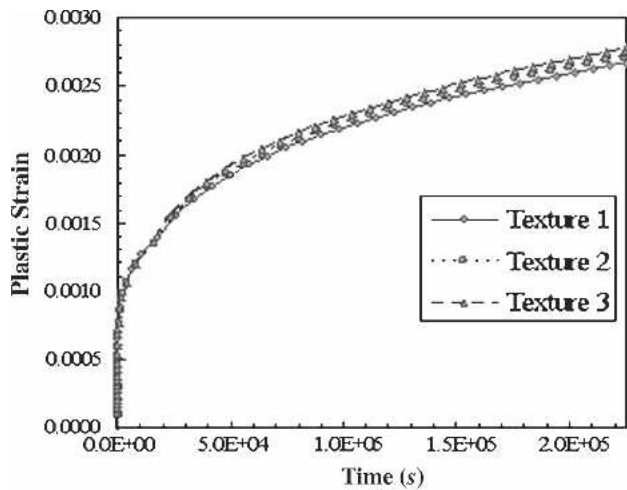

Fig. 15—Comparison of the stress normal to the basal plane in three representative grains.

1, 2, and 3 correspond to those generated by OPAM, OPAM + MPAM, and OPAM + MPAM + MTPAM, respectively. Comparison of the macroscopic stress-strain plots for the short-term constant strain rate tests, both in tension and compression, shows almost no dependence on the microstructure. However, the macroscopic responses for long-term creep tests have significant dependence on the microstructure (Figure 16). There is considerable difference in the creep strain for different microtextures, both for tension and compression creep. The creep strain progressively increases with better matching of the OIM-based microtexture data. With increasing accuracy of microtexture representation, more and more low-angle grain boundaries are added. A cluster of similarly oriented grains tend to creep more than dissimilarly oriented neighboring grains. Finally, the highest basal normal stresses σ_n^τ arising in the microstructures for compression creep with the three variant microtextures are plotted in Figure 17. The highest σ_n^τ with time for the OPAM + MPAM + MTPAM-generated computational models increases faster than those for the other microstructures. Both the equivalent microtexture and equivalent MOD + OD-based microstructures yield considerably higher stresses than just the equivalent OD-based microstructure. Thus, the correct representation of the microstructure, especially with respect to misorientation and microtexture distribution, is critical in identifying local hot spots and developing a criterion for crack initiation in creeping polycrystalline materials.

IX. CONCLUSIONS

This paper is aimed at a systematic development of an experimentally validated crystal plasticity-based computational model of α/β processed Ti-6242. The model has the capability of making predictions on the effect of microstructural stress-strain evolution and localization, especially leading to crack initiation. A rate-dependent elasto-crystalplasticity model is incorporated in this model to accommodate anisotropy in material behavior and tension-compression asymmetry inherent to this alloy. The Ti-6242 microstructure consists of two major phases: a primary α phase of equiaxed Ti-6Al grains and a transformed β phase that consist of α/β laths in colony structure. A combination of microtesting, OIM, computational simulations, and minimization process involving GA is implemented in this study for careful characterization and calibration of material parameters. Elastic and crystal plasticity parameters for individual phases and crystal slip systems are determined by this process. Relevant parameters are further adjusted to account for size effects in the polycrystalline microstructure. Such a detailed material characterization for this alloy is scarce in literature. A particularly important development is the creation of a homogenized equivalent model of the transformed β colonies for incorporation in the Ti-6242 FE model. The polycrystalline Ti-6242 computational model is subsequently constructed to incorporate accurate phase volume fractions, as well as orientation distributions that are statistically equivalent to those observed in OIM scans. The effects of accurate orientation, misorientations, and microtexture distributions are investigated through simulations using this computational model. The polycrystalline FE model is validated by comparing the results of simulations

(a)
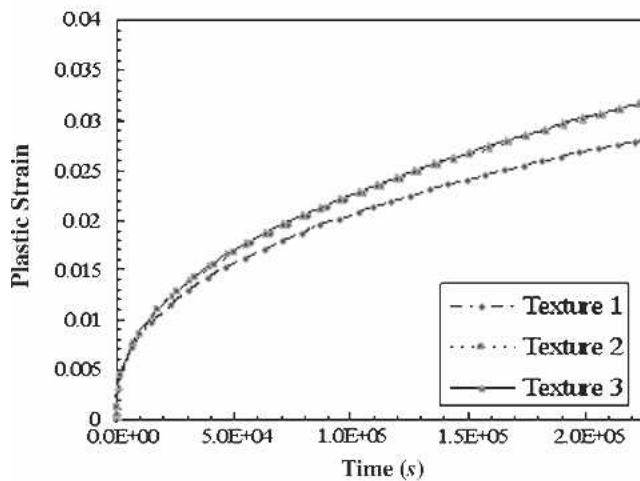
(b)

Fig. 16—Comparison of macroscopic stress-strain behavior for creep tests with the three variants in microtexture for (a) compression and (b) tension.
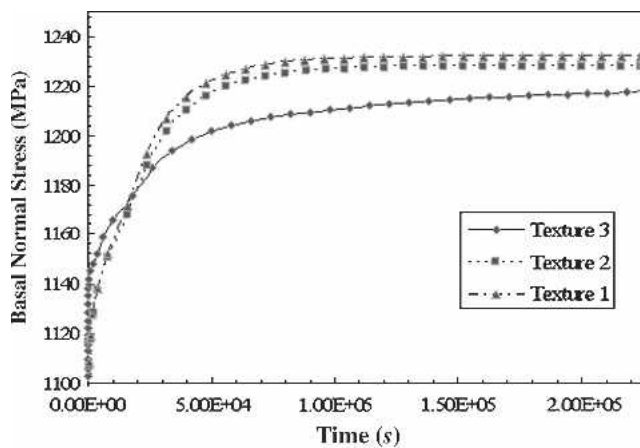

Fig. 17—Evolution of the maximum stress, normal to the basal plane for the highest stressed grain in the compression creep test, for three statistically equivalent microtextures.

with experimental data on constant strain rate and creep tests with excellent agreement.

For postvalidation exercises, the predictive capability of this model in determining microstructural stress-strain evolution is evaluated. Two particular effects—local orientation distributions and load shedding—are investigated. The stress in the loading direction and that normal to the basal plane are important variables governing dwell fatigue crack initiation that are examined. For compression creep simulation, the distributions of these stresses are evaluated along different sections of the computational domain. In all these section plots, it is observed that the local stresses can reach much higher values than the applied creep load due to high $<c + a>$ activity and load shedding from neighboring grains. The evolution of the plastic strain along these sections shows significant nonuniform distribution in this heterogeneous "composite"-type material. Finally, simulations with three different microstructural orientation distributions provide a good understanding of the role of precise microstructure representation on the development of local variables likes stresses or strains. Creep test simulations show a very high degree of microstructural dependence, even for the macroscopic response. The average creep strain is higher with a representation of the experimental microtexture. This can be attributed to an increasing amount of soft clustered regions of similar orientations with progressively better matching of actual texture. Plots of stresses normal to the basal plane also show significantly higher stresses for microstructures with matched misorientations and microtexture. Accurate representation of the microstructure in an FE model is of high importance in the identification of crack initiation sites. Current activities in the corresponding author's group are dedicated toward better methods of extracting microstructural information in computational models. This paper provides a good understanding of Ti-6242 from a local viewpoint and provides the potential for its being used for developing fatigue failure criteria.

REFERENCES

1. F.H. Froes, ed.: *Non-Aerospace Applications of Titanium*, TMS, Warrendale, PA, 1998.

2. M.A. Imam and C.M. Gilmore: *Metall. Trans. A*, 1979, vol. 10A, pp. 419-25.
3. H.P. Chu: *J. Mater.*, 1970, vol. 5, pp. 633-42.
4. B.C. Odegard and A.W. Thompson: *Metall. Trans.*, 1974, vol. 5, pp. 1207-13.
5. W.H. Miller, R.T. Chen, and E.A. Starke: *Metall. Trans. A*, 1987, vol. 18A, pp. 1451-67.
6. T. Neeraj, D.H. Hou, G.S. Daehn, and M.J. Mills: *Acta Mater.*, 2000, vol. 48, pp. 1225-38.
7. T. Neeraj and M.J. Mills: *Mater. Sci. Eng. A*, 2001, vol. 319, pp. 415-19.
8. A.W. Thompson and B.C. Odegard: *Metall. Trans.*, 1973, vol. 4, pp. 899-908.
9. S. Balasubramanian and L. Anand: *Acta Mater.*, 2002, vol. 50, pp. 133-48.
10. G.B. Sarma and P.R. Dawson: *Acta Mater.*, 1996, vol. 40, pp. 1937-53.
11. P.R. Dawson and E.B. Marin: *Adv. Appl. Mech.*, 1998, vol. 34, pp. 77-169.
12. D.P. Mika and P.R. Dawson: *Mater. Sci. Eng. A*, 1998, vol. 257, pp. 62-76.
13. D. Pierce, R.J. Asaro, and A. Needleman: *Acta Metall. Mater.*, 1983, vol. 31, pp. 1951-75.
14. R.J. Asaro and A. Needleman: *Scripta Metall. Mater.*, 1984, vol. 18, pp. 429-35.
15. S.V. Harren and R.J. Asaro: *J. Mech. Phys. Solids*, 1989, vol. 37, pp. 191-232.
16. C.L. Xie, S. Ghosh, and M. Groeber: *J. Eng. Mater. Tech.*, 2004, vol. 126, pp. 339-52.
17. S.R. Kalidindi, C.A. Bronkhorst, and L. Anand: *J. Mech. Phys. Solids*, 1992, vol. 40, pp. 537-69.
18. M. Kothari and L. Anand: *J. Mech. Phys. Solids*, 1998, vol. 46, pp. 51-67.
19. M. Grujicic and S. Batchu: *J. Mater. Sci.*, 2001, vol. 36, pp. 2851-63.
20. O.K. Kad, M. Dao, and R.J. Asaro: *Mater. Sci. Eng. A*, 1995, vol. 192–193, pp. 97-103.
21. A. Staroselsky and L. Anand: *Int. J. Plasticity*, vol. 19, 2003, pp. 1843-60.
22. O. Diard, S. Leclercq, G. Rousselier, and G. Cailletaud: *Int. J. Plasticity*, vol. 21, 2005, pp. 691-722.
23. T. Buchheit, G. Wellman, and C. Battaile: *Int. J. Plasticity*, vol. 21, 2005, pp. 221-49.
24. R.E. Loge, H.S. Turkmen, M.P. Miller, R. Rogge, and P.R. Dawson: *Model. Simulation Mater. Sci. Eng.*, vol. 12, 2004, pp. 633-63.
25. S. Li, P.V. Houtte, and S. Kalidindi: *Model. Simulation Mater. Sci. Eng.*, vol. 12, 2004, pp. 845-70.
26. A.A. Salem, S.R. Kalindidi, and S.L. Semiatin: *Acta Mater.*, vol. 53, 2005, pp. 3495-502.
27. V. Hasija, S. Ghosh, M.J. Mills, and D.S. Joseph: *Acta Mater.*, 2003, vol. 51, pp. 4533-49.
28. M.F. Savage: Ph.D. Dissertation, The Ohio State University, Columbus, OH, 2000.
29. S. Suri, G.B. Vishwanathan, T. Neeraj, D.H. Hou, and M.J. Mills: *Acta Mater.*, 1999, vol. 47, pp. 1019-34.
30. C.A. Bronkhorst, S.R. Kalidindi, and L. Anand: *Philos. Trans. R. Soc. London, Ser. A*, 1992, vol. 341, pp. 443-77.
31. S. Harren, T.C. Lowe, R.J. Asaro, and A. Needleman: *Philos. Trans. R. Soc. London, Ser. A*, 1989, vol. 328, pp. 443-500.
32. ABAQUS reference manuals: Hibbit, Karlsson and Sorenson, Inc., Providence, RI, 2001.
33. M.F. Savage, J. Tatalovich, and M.J. Mills: *Philos. Mag. A*, 2004, vol. 84 (11), pp. 1127-54.
34. M.F. Savage, J. Tatalovich, M.D. Uchic, M. Zupan, K.J. Hemker, and M.J. Mills: *Mater. Sci. Eng. A*, 2001, vol. 319–321, pp. 398-403.
35. T. Neeraj, M.F. Savage, J. Tatalovich, L. Kovarik, R.W. Hayes, and M.J. Mills: *Philos. Mag.*, 2005, vol. 85 (2–3), pp. 279-95.
36. V. Sinha, M.J. Mills, and J.C. Williams: *Metall. Trans. A*, 2004, vol. 35A, pp. 3141-48.
37. D. Goldberg: *Genetic Algorithm in Search Optimization and Machine Learning,* 1st ed., Addison Wesley, Reading, MA, 1989.
38. D.L. Carroll: *AIAA J.*, 1996, vol. 34, pp. 338-46.
39. D. Roundy, C.R. Krenn, L. Marvin, L. Cohen, and J.W. Morris: *Philos. Mag. A*, 2001, vol. 81, pp. 1725-47.
40. G.I. Taylor: *J. Inst. Metals*, 1938, vol. 62, pp. 307-24.
41. C.L. Xie and E. Nakamachi: *J. Mater. Process Tech.*, 2002, vol. 122, pp. 104-11.
42. A. Kumar and P.R. Dawson: *Comput. Methods Appl. Mech. Eng.*, 1992, vol. 153, pp. 153-259.
43. U.F. Kocks, C.N. Tomé, and H.R. Wenk: *Texture and Anisotropy: Preferred Orientations in Polycrystals and Their Effect on Materials Properties*, Cambridge University Press, Cambridge, 1998.
44. A.P. Woodfield, M.D. Gorman, R.R. Corderman, J.A. Sutliff, and B. Yamrom: *Titanium '95: Science and Technology*, 1995, pp. 1116-24.
45. D. Norfleet: The Ohio State University, Columbus, OH, unpublished research, 2005.
46. M.R. Bache and W.J. Evans: *J. Eng. Gas Turbines and Power*, 2003, vol. 125, pp. 241-45.
47. A. Arsenlis and D.M. Parks: *Acta Mater.*, 1999, vol. 47 (5), pp. 1597-611.
48. L.P. Evers: Ph.D. Dissertation, TU Eindhoven, Eindhoven, The Netherlands, 2003.